Cell Reports

Article

Schizophrenia-associated complement C4 impairs synaptic connectivity and decreases microglia-synapse interactions through CR3 signaling

Graphical abstract

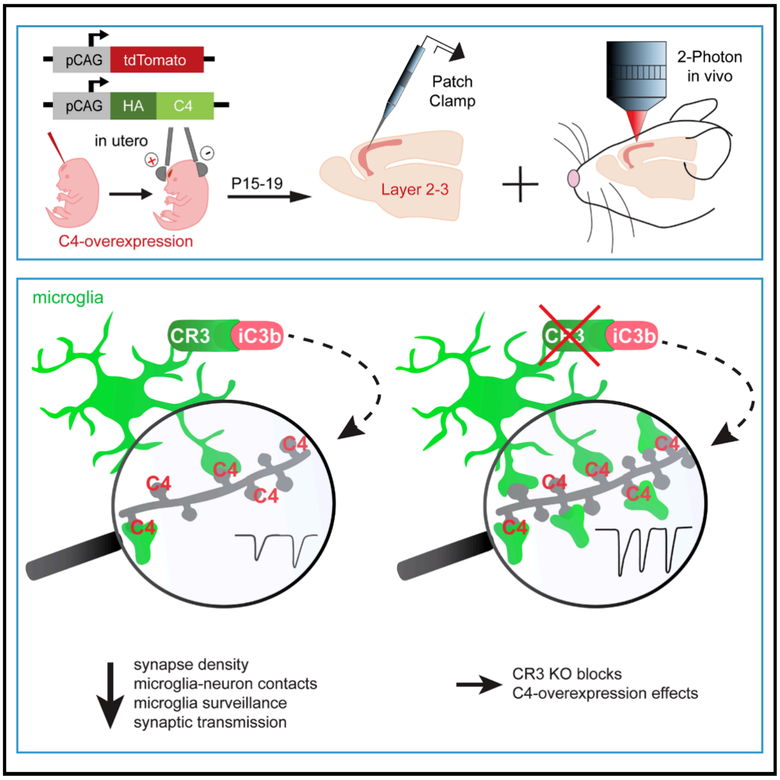

Highlights

- Complement C4 overexpression (C4-OE) reduces cortical synapse density and function
- Complement receptor 3 (CR3) is required for synaptic deficits caused by C4-OE
- C4-OE lowers microglial surveillance and microglia-neuron contacts *in vivo*
- CR3 deficiency normalizes microglial surveillance and microglia-neuron contacts

Authors

Nala Gockel, Nayadoleni Nieves-Rivera,
Mélanie Druart, ..., Baiba Jansone,
Martin Fuhrmann,
Corentin Le Magueresse

Correspondence

martin.fuhrmann@dzne.de (M.F.),
corentin.le-magueresse@inserm.fr
(C.L.M.)

In brief

Genetic risk for schizophrenia has been linked to high expression of complement C4, but the mechanism remained unclear. Gockel et al. show that microglial CR3 receptors mediate the effects of elevated C4 expression in the mouse cortex, including altered synapse density and function, decreased microglial motility, and reduced microglia-neuron contacts.

Gockel et al., 2026, Cell Reports *45*, 117161
April 28, 2026 © 2026 The Authors. Published by Elsevier Inc.
https://doi.org/10.1016/j.celrep.2026.117161

CellPress

Cell Reports

CellPress
OPEN ACCESS

Article

Schizophrenia-associated complement C4 impairs synaptic connectivity and decreases microglia-synapse interactions through CR3 signaling

Nala Gockel,[1,5] Nayadoleni Nieves-Rivera,[2,5] Mélanie Druart,[2] Külli Jaako,[3] Falko Fuhrmann,[1] Fabrizio Musacchio,[1] Henrike Antony,[1] Manuel Mittag,[1] Sophie Crux-Daseking,[1] Stefanie Poll,[1] Baiba Jansone,[4] Martin Fuhrmann,[1,6,*] and Corentin Le Magueresse[2,6,7,*]

[1]Neuroimmunology and Imaging Group, German Center for Neurodegenerative Diseases (DZNE), Bonn, Germany

[2]Sorbonne Université, CNRS, INSERM, Institut de Biologie Paris Sorbonne, Center for Neuroscience at Sorbonne Université, Paris 75005, France

[3]Department of Pharmacology, Institute of Biomedicine and Translational Medicine, University of Tartu, 19 Ravila Street, Tartu 50411, Estonia

[4]University of Latvia, Department of Neuromedicine and Neuroscience-Faculty of Medicine, Riga 1004, Latvia

[5]These authors contributed equally

[6]These authors contributed equally

[7]Lead contact

*Correspondence: martin.fuhrmann@dzne.de (M.F.), corentin.le-magueresse@inserm.fr (C.L.M.)

https://doi.org/10.1016/j.celrep.2026.117161

SUMMARY

High-expression variants of the complement C4 gene increase schizophrenia (SZ) risk. C4 overexpression (C4-OE) in the mouse frontal cortex recapitulates SZ-associated phenotypes, including lower synapse density, but the underlying mechanisms remain unclear. In the complement cascade, C4 is upstream of C3, whose cleavage fragments can bind complement receptors, including CR3, selectively expressed by microglia in the brain parenchyma. Therefore, we hypothesize that microglial CR3 mediates C4-OE effects. We show that C4-OE alters synapse density and function and that these effects are rescued in CR3-deficient mice. Contrary to the models of excessive microglia-mediated synaptic elimination, our previous results indicate that C4-OE reduces spine formation and elimination. Here, using *in vivo* two-photon imaging, we find that C4-OE decreases microglial surveilled volume, motility, and the frequency of microglial contacts with pre- and postsynaptic structures. These changes are abolished by CR3 deficiency. Our findings suggest that CR3-mediated modulation of microglia-synapse interactions underlies C4-OE effects relevant to SZ.

INTRODUCTION

Schizophrenia (SZ) is a severe neurodevelopmental disorder characterized by psychosis, emotional flattening, and cognitive deficits, with a typical onset of psychosis between late adolescence and early adulthood. Negative and cognitive symptoms, in particular, are thought to reflect abnormalities in cortical function.[1] Disturbances in synaptic refinement, a process by which neural circuits are fine-tuned in the maturing brain, have long been proposed to be involved in the etiology of SZ. Supporting this hypothesis, histological and brain imaging studies have reported reduced volume of gray matter and decreased synapse density in the cortical areas in patients with SZ compared with healthy individuals.[2–4] However, the cellular and molecular mechanisms underlying these deficits are still unclear.

SZ is a highly heritable disease. Genome-wide association studies have consistently shown that the major histocompatibility complex (MHC) region on chromosome 6 presents the strongest genetic association with SZ.[5] The gene encoding complement component 4 (C4) is located within the MHC region and exists as two functionally distinct isoforms, *C4A* and *C4B*, which exhibit copy number variation. Alleles conferring high expression of C4A correlate with an increased risk of SZ.[6] Mouse C4 is encoded by a single gene, which shares similarities with both human *C4A* and *C4B* isoforms. Several experimental models have been developed to study the effects of elevated C4 expression on neuronal development and function. The elevated expression of human C4A in induced pluripotent stem cell-derived neurons or in mice, as well as mouse C4 overexpression (C4-OE) in the mouse cortex, was shown to induce SZ-associated phenotypes, including decreased glutamatergic and inhibitory synaptic transmission, NMDA receptor (NMDAR) hypofunction, decreased dendritic spine density, and altered social and cognitive behaviors in mice.[7–10]

Microglial cells influence synaptic remodeling by engaging with developing neurons through various receptor-ligand interactions, including complement receptors. A long-standing hypothesis proposes that microglial cells control the pruning of supernumerary synapses during postnatal brain maturation and in adulthood, in particular, by detecting complement-tagged synapses for elimination.[11] Several lines of evidence indicate that microglia-mediated synaptic elimination plays a crucial role in maintaining the brain's normal functions, such as vision[12,13] and sleep.[14] Conversely, microglia-neuron interactions have also been shown to promote dendritic spine formation.[15–17] In addition, microglia-neuron interactions shape functional synaptic properties, such as glutamate release probability and the ratio of AMPA and NMDA receptors at synapses.[18–20] Smaller dendritic spine density in mouse models of elevated C4 expression has been attributed to enhanced phagocytosis of synaptic structures by microglial cells.[9] While we confirmed through *in vivo* two-photon microscopy that C4-OE indeed results in lower dendritic spine density, our findings revealed an unexpected pattern: the reduced density correlated with diminished rates of both spine formation and elimination, rather than heightened elimination, suggesting that a spine formation deficit could be the result of C4-OE. Whether and how microglia are involved in mediating these structural and functional synaptic alterations resulting from elevated C4 expression remains to be elucidated.

C4 is central to the classical complement cascade, which, in addition to supporting host defense, also plays a role in synaptic refinement in mammals.[21] Complement molecules are synthesized and released by both neuronal and glial cells within the central nervous system.[22] The activation of the complement cascade leads to the cleavage of complement C3 into two proteolytic fragments, C3a and C3b. The cleavage of C3b by factor I forms iC3b (Figure 1A). Microglia are the resident macrophages of the brain parenchyma and selectively express CR3, the receptor for iC3b.[23–25] Microglial CR3 plays a central role in the refinement of neuronal connectivity in the neonatal retino-geniculate system.[25] However, its role in synapse remodeling in the cortex is less clear. In particular, in mice lacking CR3, dendritic spine density was not altered in layer 5 neurons of the prelimbic cortex, while perinatal elimination of neurons was impaired, leading to increased cortical thickness in adulthood.[26]

Here, we explored whether CR3 receptors mediate synaptic alterations caused by C4-OE and investigated how microglial properties and microglia-synapse interactions were altered in response to C4-OE. We found that C4-OE induced changes in excitatory and inhibitory synaptic activity, spine density, and NMDAR function. All these effects were normalized in CR3-deficient mice, suggesting that CR3 is required for the pathological consequences of C4-OE. To further investigate the effect of C4-OE on microglia-synapse interactions, we used *in vivo* two-photon microscopy. The motility of microglial fine processes and volume surveilled by microglia were decreased in response to C4-OE, along with a strong decrease in contact frequency between microglia and post- as well as presynaptic structures. The effect of C4-OE on microglial surveillance and microglia-synapse interactions was abolished in CR3 knockout (KO) mice. These results indicate that microglial CR3 plays a key role in shaping microglia-synapse communication in the context of C4-OE and suggest that C4-OE may decrease synapse formation by reducing microglia-synapse interactions.

RESULTS

CR3 receptors mediate synaptic dysfunctions caused by C4-OE in layer II–III pyramidal neurons

We first sought to compare the consequences of C4-OE on synaptic properties in wild-type (WT) and CR3 KO mice. Using *in utero* electroporation in WT and CR3 KO mice at embryonic day 14.5 (E14.5), we selectively transfected progenitors of the frontal cortex (FC) layer II–III pyramidal cells with either a plasmid expressing tdTomato (tdTom, control condition) or a combination of the same tdTom-expressing plasmid and a C4-OE plasmid encoding mouse C4 with an N-terminal HA tag (C4HA plasmid, Figure 1B). The expression of tdTom enabled the visualization of electroporated cells. Immunochemistry for tdTom and HA confirmed that tdTom+ neurons were also HA+ in the C4-OE condition (Figures S1A and S1B).

We used whole-cell patch-clamp in visually identified (tdTom+) layer II–III pyramidal cells from the FC of mice aged P15–P19, after the peak of dendritic spine turnover in neocortex,[27–29] to record miniature excitatory postsynaptic currents (mEPSCs) and measure the effect of C4-OE on functional synaptic transmission. C4-OE significantly decreased mEPSC frequency in WT mice, in line with previous results,[8,10] but did not induce changes in CR3 KO mice (Figures 1C and 1D). C4-OE also significantly decreased the amplitude of mEPSCs in WT mice but not in mice lacking CR3 (Figure 1E). C4-OE significantly lowered the coefficient of variation (CV) of mEPSC amplitude in WT mice, but this effect was absent in CR3 KO mice, where a small increase was observed (Figure S2). A lower CV could be due to reduced variability in quantal presynaptic release, but it might also stem entirely from a postsynaptic effect, because the variation in mEPSC amplitude can arise from variability in postsynaptic receptor properties such as receptor density or number. We had previously shown that the paired-pulse ratio (PPR) of evoked postsynaptic currents (PSCs), a parameter sensitive to presynaptic changes in release probability, does not change in response to C4-OE across three different stages of postnatal development.[10] Taken together, these findings suggest that C4-OE reduces functional excitatory inputs, resulting mainly in postsynaptic alterations and changes in the number of functional excitatory synapses in WT mice, and that these changes are prevented in CR3 KO mice.

C4-OE causes NMDAR hypofunction,[10] a phenotype frequently associated with SZ.[30] To investigate whether CR3 receptors are implicated in the effects of C4-OE on NMDAR-mediated transmission, we measured the AMPA/NMDA ratio of evoked EPSCs in control and C4-OE neurons from WT and CR3-deficient mice. We found that C4-OE increased the AMPA/NMDA ratio in WT mice (Figures 1F and 1G). Since mEPSC amplitude was decreased in C4-OE cells, indicative of decreased AMPAR-mediated transmission (Figure 1E), the increased AMPA/NMDA ratio reflects a specific NMDAR hypofunction at excitatory synapses onto C4-OE pyramidal cells. In contrast, the AMPA/NMDA ratio was similar in C4-OE and control pyramidal cells in CR3 KO mice (Figures 1F and 1G). Because variations in the decay time constant of NMDAR-mediated currents, which depend on the subunit composition of NMDARs, may affect the measurement of the AMPA/NMDA ratio, we verified that the decay kinetics of NMDAR-mediated currents were similar across all groups (Figure 1H).

To investigate whether CR3 mediates the effect of C4-OE on inhibitory transmission, we recorded miniature inhibitory postsynaptic currents (mIPSCs) in P15–P19 electroporated WT and CR3 KO mice. C4-OE in WT mice resulted in decreased mIPSC

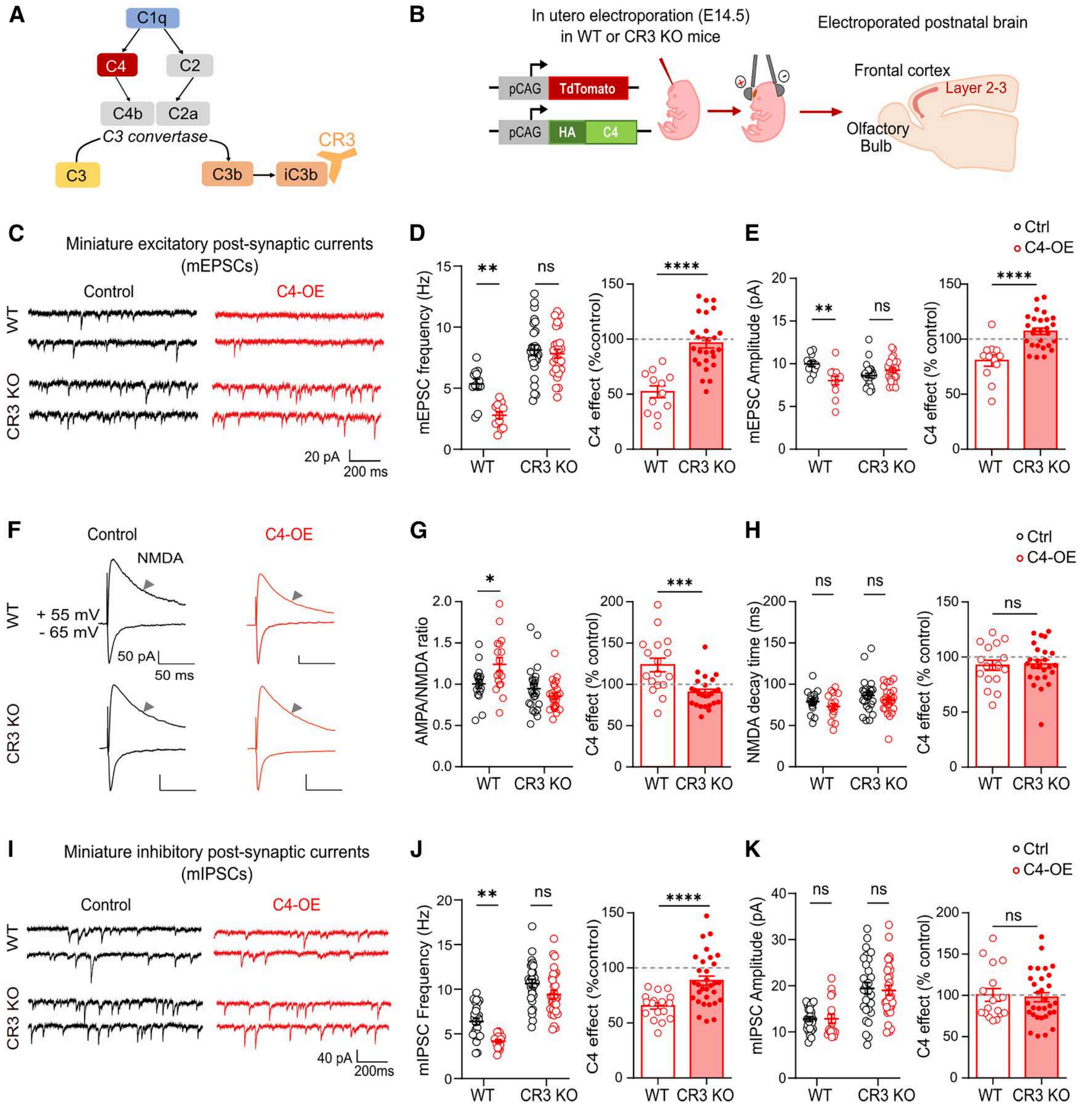

Figure 1. C4-OE alters synaptic properties in WT but not in CR3 KO mice

(A) Simplified diagram of the classical complement cascade, including iC3b and its receptor CR3.

(B) Left: plasmids used for control *in utero* electroporation (tdTomato) and C4 overexpression (tdTomato and HA-tagged C4). Middle: *in utero* electroporation procedure targeting neural progenitors of layer II–III pyramidal cells. Right: location of electroporated neurons in the postnatal brain.

(C) Sample traces of mEPSCs in WT and CR3 KO mice.

(D) Dot plot of mEPSC frequencies in WT and CR3 KO mice (Sidak's test, $^{**}p = 0.0025$) and histogram summarizing the effect of C4-OE in each genotype (*t* test, $^{****}p < 0.0001$).

(E) Dot plot of mEPSC amplitudes (Dunn's test, $^{**}p = 0.0014$) and effect of C4-OE in each genotype (*t* test, $^{****}p < 0.0001$). ctrl WT: $n = 12$ cells, $N = 4$ mice; C4- OE WT: $n = 12$ cells, $N = 5$ mice; ctrl CR3 KO: $n = 28$ cells, $N = 8$ mice; and C4-OE CR3 KO: $n = 27$ cells, $N = 6$ mice.

(F) Representative traces of EPSCs recorded in WT and CR3 KO mice to measure AMPA and NMDA currents evoked by an electrical stimulation. The NMDA current was measured at +55 mV, 50 ms after stimulation (gray arrowheads).

(G) Dot plot of AMPA/NMDA ratio (Sidak's test, $^{*}p = 0.0167$) and effect of C4-OE in each genotype (*t* test; $^{***}p = 0.0002$).

(H) Dot plot of AMPA/NMDA ratio (Dunn's test, ns: $p > 0.05$) and effect of C4-OE in each genotype (*t* test; ns: $p = 0.844$). ctrl WT: $n = 17$ cells, $N = 5$ mice; C4-OE WT: $n = 17$ cells, $N = 5$ mice; ctrl CR3 KO: $n = 24$ cells, $N = 8$ mice; and C4-OE CR3 KO: $n = 25$ cells, $N = 6$ mice).

(I) Sample traces of mIPSCs in WT and CR3 KO mice.

(J) Dot plot of mIPSC frequencies (Sidak's test, $^{**}p = 0.0026$) and effect of C4-OE in each genotype (*t* test, $^{***}p = 0.004$).

(K) Dot plot of mIPSC amplitudes (Dunn's test, ns: $p > 0.05$) and effect of C4-OE in each genotype (Mann-Whitney test, ns: $p = 0.98$). control WT: $n = 26$ cells, $N = 8$ mice; C4-OE WT: $n = 17$ cells, $N = 6$ mice; control CR3 KO: $n = 28$ cells, $N = 8$ mice; and C4-OE CR3 KO: $n = 31$ cells, $N = 7$ mice).

Data are presented as mean ± SEM error bars. Each dot represents a single recorded cell. ns: $p > 0.05$, not significant.

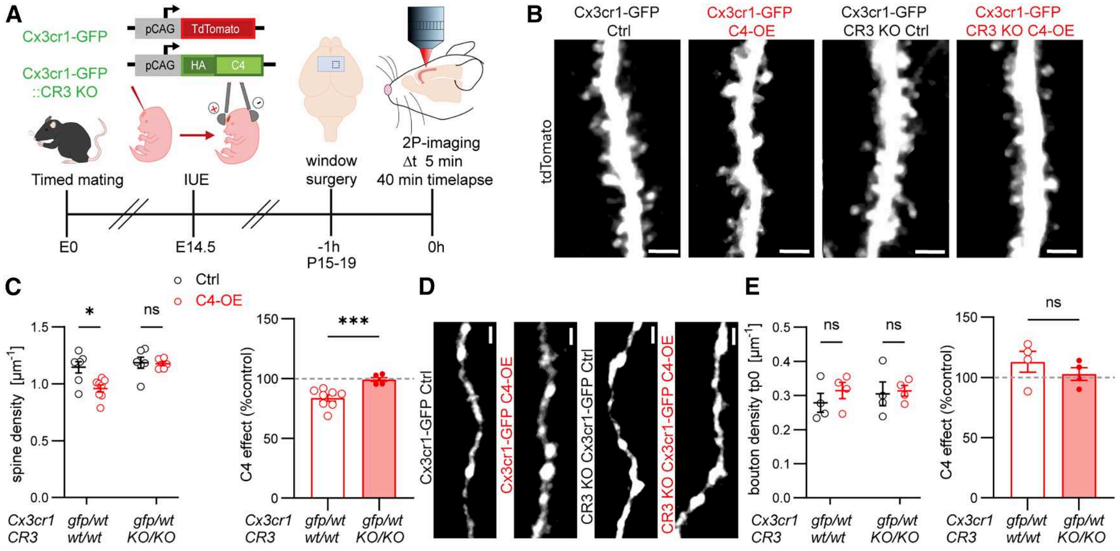

Figure 2. C4-OE-induced decrease in dendritic spine density is absent in CR3 KO mice *in vivo*

(A) Schematic representation of the experimental timeline for *in vivo* imaging.

(B) Representative dendrite sections for the four experimental groups. Scale bars, 3 μm.

(C) Left: quantification showing that C4-OE significantly decreases spine density in control Cx3cr1-GFP mice but not in Cx3cr1-GFP::CR3 KO mice. (Dunn's test, Cx3cr1-GFP mice $^*p = 0.0135$). Ctrl Cx3cr1-GFP, $N = 7$ mice; C4-OE Cx3cr1-GFP, $N = 8$ mice; Ctrl Cx3cr1-GFP::CR3 KO, $N = 6$ mice; and C4-OE Cx3cr1-GFP::CR3KO, = 6 mice. Right: histogram showing that the effect of C4-OE on spine density significantly differs across genotypes (Mann-Whitney test, $^{***}p = 0.0007$, ns: $p > 0.05$).

(D) Representative axonal sections for the four experimental groups. Scale bars, 2 μm.

(E) Left: quantification showing that C4-OE did not significantly alter axonal bouton density in either genotype (Dunn's test, Ctrl Cx3cr1-GFP, $N = 4$ mice; C4-OE Cx3cr1-GFP, $N = 4$ mice; Ctrl Cx3cr1-GFP::CR3 KO, $N = 4$ mice; and C4-OE Cx3cr1-GFP::CR3 KO, $N = 4$ mice). Right: histogram showing the effect of C4-OE in both genotypes (Mann-Whitney test, ns: $p > 0.05$).

Data are presented as mean ± SEM error bars. Each dot represents the mean value for a single mouse. Two to 3 dendrites and 2 axons were imaged in each mouse. ns: $p > 0.05$, not significant.

frequency, but not amplitude, in layer II–III pyramidal cells. In contrast, C4-OE in CR3 KO mice did not alter the frequency and amplitude of mIPSCs, indicating that CR3 receptors also mediate the detrimental effects of C4-OE on inhibitory transmission (Figures 1I–1K).

Altogether, these results demonstrate that C4-OE impairs both excitatory and inhibitory synaptic transmission primarily through CR3-dependent mechanisms.

CR3 receptors are required for the effects of C4-OE on dendritic spines

C4-OE induces reduced dendritic spine density in layer II–III neurons of the FC.[8,10] To assess whether CR3 mediates the effects of C4-OE on spine density, we used *in vivo* two-photon imaging and studied the density of dendritic spines in layer II–III neurons in the FC of *in utero*-electroporated mice at P15–P19 (Figure 2A). To simultaneously visualize microglia in the same mice, we used *in utero* electroporation of either the tdTomato plasmid (control group) or tdTomato+C4HA plasmids (C4-OE condition) in Cx3cr1$^{gfp/wt}$ transgenic mice expressing GFP in microglia (henceforth referred to as Cx3cr1-GFP; see STAR Methods). Additionally, we performed similar *in utero* electroporations of tdTomato (control) or tdTomato+C4HA plasmids (C4-OE) in Cx3cr1$^{gfp/wt}$::CR3$^{ko/ko}$ double transgenic mice lacking CR3 receptors (henceforth referred to as Cx3cr1-GFP::CR3 KO; see STAR Methods; the evaluation of microglia based on GFP expression will be presented in subsequent sections). We found that C4-OE decreased spine density by 16.5% in Cx3cr1-GFP mice *in vivo*. The effect of C4-OE on spine density was abolished in Cx3cr1-GFP::CR3 KO mice (Figures 2B and 2C). In addition to postsynaptic dendritic spines, we also measured the density of axonal boutons of C4-OE neurons. C4-OE did not change the density of axonal boutons, neither in Cx3cr1-GFP nor in Cx3cr1-GFP::CR3 KO mice (Figures 2D and 2E). To confirm that the effect of C4-OE on spine density was mediated by CR3, we also imaged isolated dendritic fragments in layer II–III using confocal imaging of tdTom+ cells in fixed brain slices from P15–P19 WT and CR3 KO mice. In agreement with previous results,[8,10] we found that C4-OE reduced spine density by 22.4% in pyramidal cells from WT mice. In contrast, C4-OE did not change spine density in CR3 KO mice (Figures S3A and S3B). Morphological parameters of dendritic spines—length, maximum head diameter, and the ratio of mean head to neck diameters—were plotted in three dimensions (Figure S3C). Unsupervised clustering, based on Euclidean distance in the parameter space, identified three distinct spine populations, which resemble commonly recognized categories of dendritic spines described in the literature: "thin," "small/stubby," and "mushroom-like." The relative distribution of spines in these three clusters remained similar across all experimental conditions (Figure S3D).

Taken together, these results indicate that microglial CR3 receptors are necessary for the effects of C4-OE on dendritic spine density and synaptic transmission. Furthermore, C4-OE and CR3-mediated signaling seem to selectively affect the density of spines rather than the density of axonal boutons.

C4-OE DOES NOT SIGNIFICANTLY AFFECT SYNAPTIC MATERIAL ENGULFMENT OR MICROGLIA DENSITY

In the CNS, CR3 is exclusively expressed by microglia. Furthermore, the role of microglia in neural circuit refinement has been extensively documented, and previous studies suggested that cortical microglial cells engulf more synaptic material in response to elevated C4 expression.[8,9] Therefore, we set out to investigate the morphology and engulfment capacity of microglial cells in response to C4-OE in WT and CR3 KO mice. Firstly, we aimed to determine whether C4-OE-induced phenotypes are caused by imbalances in phagocytosis of synaptic material by microglia. We co-immunostained microglia for Iba1, lysosomes for CD68, and pre- as well as postsynaptic structures for Bassoon and Homer1, respectively. C4-OE did not alter the volume of CD68$^+$ microglial lysosomes in either WT or CR3 KO mice aged P15–P19. The number of Bassoon and Homer1 puncta within CD68$^+$ microglial lysosomes was also similar in all experimental groups (Figures 3A–3D). To validate these findings using an additional synaptic marker, we examined the engulfment of synaptophysin-positive presynaptic structures in microglia from Cx3cr1-GFP control and C4-OE mice, as well as from Cx3cr1-GFP::CR3 KO control and C4-OE mice. The analysis revealed that the number of synaptophysin puncta within microglia was comparable across all four experimental groups (Figure S4). Together, these results suggest that C4-OE did not alter the phagocytic capacities of microglia or the amount of engulfed synaptic material. Next, we investigated the density of microglia in response to C4-OE in WT and CR3-deficient mice. The density of microglial cells in the electroporated region (FC layer II–III) did not differ across experimental groups (Figures 3E and 3F). To verify that the ablation of CR3 did not cause major changes in the development and/or reactivity of microglial cells, we quantified the expression of selected proteins using immunoblotting in the FC of CR3 KO mice and WT mice aged P15–P19. Osteopontin and macrophage colony-stimulating factor 1 (CSF1) are selectively expressed by microglial cells and strongly downregulated during postnatal development (P5 to P30).[31] The expression of Osteopontin and CSF1 was not altered in CR3 KO mice compared to WT controls. The expression of microglia-specific Iba1 and TLR4, which are upregulated in "reactive" microglial cells,[32,33] were also similar in CR3 KO and WT mice (Figure S5). Together, these findings indicate that C4 overexpression does not affect microglial morphology, density, or phagocytic activity, and that CR3 deficiency does not alter microglial development or reactivity.

CR3 receptors are required for C4-OE-elicited decrease in microglia surveillance

To assess whether microglia are not only morphologically but also functionally altered by C4-OE, we performed two-photon *in vivo* imaging to measure microglia surveillance capacity. To visualize microglia, we used Cx3cr1-GFP and Cx3cr1-GFP::CR3 KO mice (P15–P19) expressing GFP in microglia. In the same mice, control or C4-OE neurons could be identified by their tdTom fluorescence. In our prior research, we investigated dendritic spine formation and elimination by employing long-interval (4 h) time-lapse microscopy.[10] Here, time-lapse *in vivo* two-photon imaging was performed for 40 min with an interval of 5 min between each acquisition to assess microglial surveillance and fine process motility (Figures 4A–4C). We quantified the volume occupied by microglia in relation to the imaged volume over the whole duration of the experiments, referred to as "surveilled volume." We found that C4-OE decreased the surveilled volume by 36% in Cx3cr1-GFP mice, whereas it had no such effect on the surveilled volume in Cx3cr1-GFP::CR3 KO mice. The effect of C4-OE on surveilled volume significantly differed between the two genotypes (Figure 4D; Video S1). Furthermore, our results show that C4-OE reduced the relative gain and loss of microglial processes in Cx3cr1-GFP mice, resulting in a 12% decrease in the turnover rate of microglial processes. In contrast, C4-OE did not change microglial fine process motility in CR3-deficient Cx3cr1-GFP mice. (Figures 4E–4G; Video S1). To investigate the downstream molecular mechanisms underlying the effect of C4-OE on microglial motility, we examined the active forms of RhoA and Rac1 in microglia. Active RhoA promotes actomyosin contractility and process retraction, whereas active Rac1 stimulates branched actin polymerization and leading-edge protrusions.[34] The amount of Rac1-GTP levels did not significantly differ within microglia across all four experimental groups (Figures S6A and S6B). However, we observed that in Cx3cr1-GFP mice with C4-OE, microglia displayed a significant increase of 40% in RhoA-GTP levels compared to those from control electroporated mice. This difference was absent in Cx3cr1-GFP::CR3 KO mice, where RhoA-GTP levels were similar between C4-OE and control conditions (Figures S6C and S6D).

These findings demonstrate that C4-OE diminishes microglial surveillance through a mechanism dependent on CR3 and suggest that the observed reduction in microglial surveillance might be partially attributed to a decrease in the motility of microglial processes involving enhanced RhoA signaling.

CR3 receptors are required for C4-OE-elicited decrease in microglia-synapse interactions

The dynamic movements of microglial processes enable them to interact with both dendrites and axons. These interactions occur at synaptic as well as non-synaptic locations. Such contact between microglia and neuronal structures may influence the formation and stabilization of new synapses and the elimination of existing ones.[12,15–17] We examined whether C4-OE altered the communication between microglia and synapses. We quantified putative microglial contacts with pre- and postsynaptic structures by time-lapse *in vivo* imaging (Figures 5A and 5B). In the same experimental groups as those used to assess microglial motility, we computed the frequency of colocalization of microglial processes with synaptic structures or dendritic shafts. We found that C4-OE significantly decreased the frequency of microglia-spine contacts by 68% in Cx3cr1-GFP mice. In addition, C4-OE significantly decreased the frequency of microglia

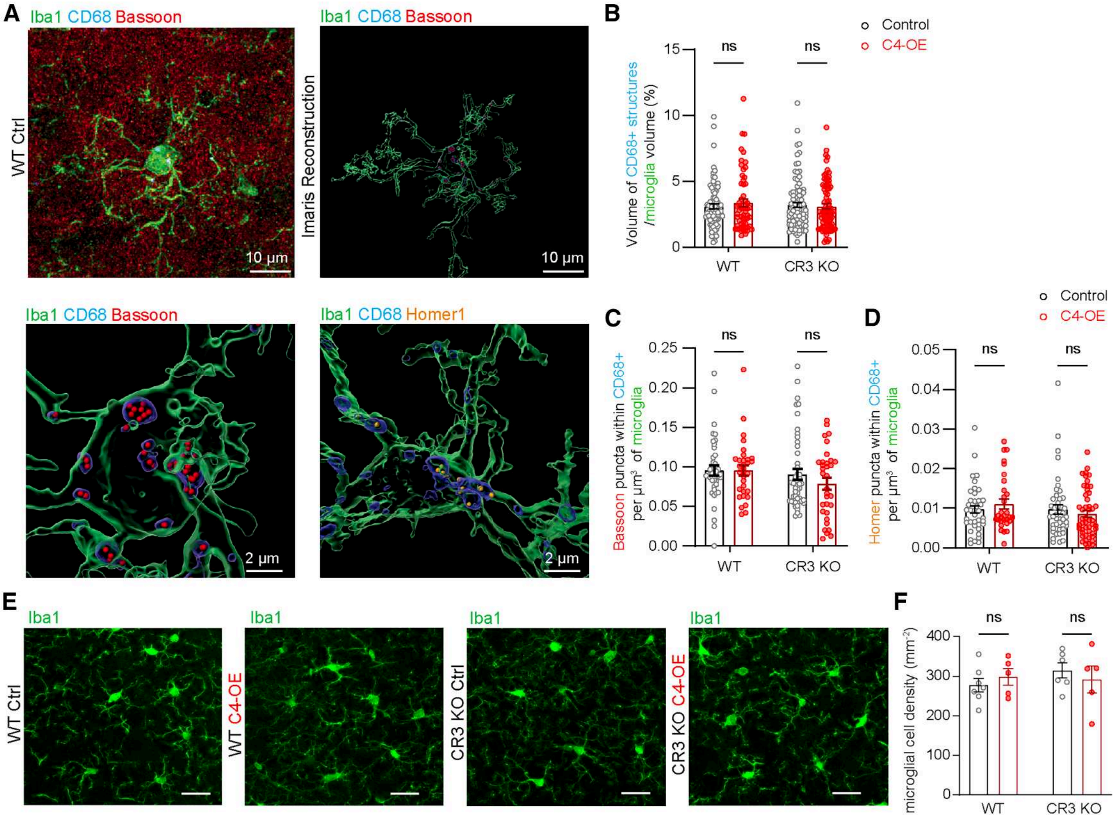

Figure 3. Microglia engulfment and density are unchanged with C4-OE and CR3 KO

(A) Representative image of an airyscan confocal image (upper left) and corresponding 3D reconstruction generated using Imaris software (upper right). Bottom: magnified 3D reconstructions showing examples of Bassoon or Homer1 puncta within CD68$^+$ structures. Scale bars, 10 μm (top) and 2 μm (bottom).

(B) Volume of CD68$^+$ structures within individual microglia, normalized to microglial volume (Dunn's test, WT: $p > 0.999$; CR3 KO: $p > 0.999$); ctrl WT: $n = 81$ microglia; C4-OE WT: $n = 61$; ctrl CR3 KO: $n = 93$; and C4-OE CR3 KO: $n = 82$.

(C) Density of Bassoon puncta inside CD68$^+$ structures per μm^3 of microglia (Dunn's test, WT: $p > 0.999$; CR3 KO: $p = 0.402$); ctrl WT: $n = 41$ microglia; C4-OE WT: $n = 31$; ctrl CR3 KO: $n = 48$; and C4-OE CR3 KO: $n = 33$.

(D) Density of Homer1 puncta inside CD68$^+$ structures within microglia, per μm^3 of microglia (Dunn's test, WT: $p > 0.999$; CR3 KO: $p > 0.999$). ctrl WT: $n = 40$ microglia; C4-OE WT: $n = 30$; ctrl CR3 KO: $n = 45$; and C4-OE CR3 KO: $n = 49$.

(E) Representative confocal acquisitions of Iba1-stained microglial cells in the FC of WT and CR3 KO mice. Scale bars, 30 μm.

(F) Microglia density histogram. C4-OE did not alter the density of Iba1+ microglial cells in either genotype. (Dunn's test, WT: $p > 0.999$; CR3 KO: $p > 0.999$) ctrl WT: $N = 7$ mice; C4-OE WT: $N = 5$ mice; ctrl CR3 KO: $N = 6$ mice; and C4-OE CR3 KO: $N = 5$ mice.

Data are presented as mean ± SEM error bars. ns: $p > 0.05$, not significant.

contacts with dendritic shafts by 76% and the frequency of microglia-axonal bouton contacts by 63%. In contrast, C4-OE did not alter microglia-spine, microglia-dendrite or microglia-bouton contacts in CR3-deficient mice (Figures 5C–5H; Videos S2 and S3). Taken together, these results demonstrate that C4-OE alters microglia-synapse communication by decreasing the frequency of contacts between microglia and pre- and post-synaptic structures as well as the frequency of contacts between microglia and non-synaptic dendritic loci. They also indicate that microglial CR3 receptors mediate C4-OE-induced changes in microglia-synapse communication.

DISCUSSION

Mouse models with elevated C4 expression display cortical phenotypes associated with SZ, including reduced dendritic spine density, diminished glutamatergic and GABAergic input, and NMDAR hypofunction. In our previous work, we demonstrated that these alterations—specifically the reduction in glutamatergic input and NMDAR hypofunction—persist from adolescence (P25–P30) through adulthood (P150–P220), highlighting the persistence of C4-OE effects.[10] The effector mechanisms remain poorly understood. Here, we found that iC3b-CR3 signaling mediates all C4-OE-induced neuronal phenotypes that were investigated, i.e., decreased frequency and amplitude of mEPSCs, reduced NMDAR-mediated synaptic transmission, and reduced frequency of mIPSCs. Since CR3 receptors are only expressed on microglia in the brain parenchyma, these results strongly suggest that microglial cells are implicated in the detrimental effects of C4-OE on synapses. Our *in vivo* two-photon imaging experiments confirmed that C4-OE alters microglial function in a CR3-dependent manner, reducing microglial

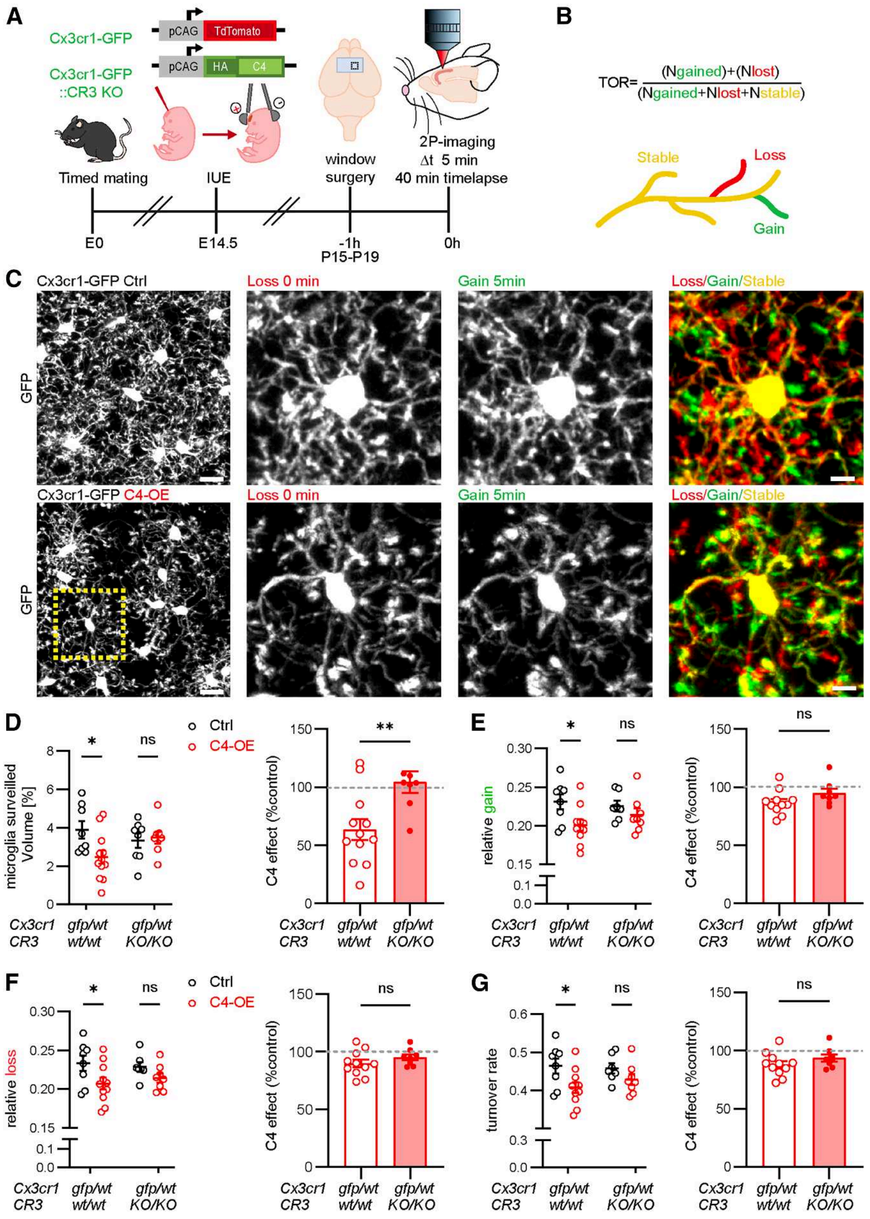

Figure 4. C4-OE-induced decrease in surveilled volume is abolished in CR3 KO mice

(A) Schematic representation of the experimental timeline for *in vivo* imaging.

(B) Formula for calculation of turnover rate (TOR) and schematic depiction of stable, lost, and gained parts of microglial processes.

(C) Representative microglia turnover examples of Ctrl Cx3cr1-GFP (upper) and C4-OE Cx3cr1-GFP mice (lower). Scale bars, 15 μm (left images) and 5 μm (right images).

(D) Average occupied volume of microglia over time calculated in per cent of a fixed-size imaging volume (100 μm × 100 μm × 50 μm). C4-OE decreased the microglia surveilled volume in Cx3cr1-GFP mice but not in Cx3cr1-GFP::CR3 KO mice (Sidak's test, *p = 0.0187, Cx3cr1-GFP Control: N = 8 mice; Cx3cr1-GFP C4-OE: N = 12 mice; CR3 KO Cx3cr1-GFP Control: N = 8 mice; and CR3KO Cx3cr1-GFP C4-OE: N = 8 mice). Additional histogram showing a significant effect of C4-OE on occupied microglia volume (unpaired t test, **p = 0.0071).

(E) Left: quantification of the relative gain of microglia process over time showing a decrease in the C4-OE group. C4-OE did not cause a similar decrease in the absence of CR3 (Šídák's test, *p = 0.0194). Right: the effect of C4-OE did not differ significantly across genotypes (Mann-Whitney test).

(F) Left: quantification showing that C4-OE decreases the relative loss of microglial processes in Cx3cr1-GFP mice but not in Cx3cr1-GFP::CR3 KO mice (Sidak's test, *p = 0.0358). Right: no significant effect of C4-OE between genotypes (Mann-Whitney test).

(G) Average total turnover rate (TOR) of microglia as calculated in (B), in the presence of absence of C4-OE. C4-OE significantly decreased the TOR in Cx3cr1-GFP mice but not in Cx3cr1-GFP::CR3 KO mice. Sidak's test, *p = 0.024). No significant effect of C4-OE between genotypes (Mann-Whitney test).

Data are presented as mean ± SEM error bars. ns: p > 0.05, not significant. Each dot represents the mean value of one mouse. (Number of mice if not stated otherwise: Cx3cr1-GFP Ctrl: N = 8 mice; Cx3cr1-GFP C4-OE: N = 11 mice; Cx3cr1-GFP::CR3KO Ctrl: N = 7 mice; and Cx3cr1-GFP::CR3KO C4-OE: N = 8 mice).

motility and surveillance. Concurrently, C4-OE increased the levels of active RhoA—a small GTPase involved in actomyosin contractility.[35] In addition, C4-OE reduced the frequency of microglia-neuron contacts at presynaptic (axonal boutons), postsynaptic (dendritic spines), and non-synaptic (dendritic shafts) sites *in vivo*. Overall, our results indicate that microglial CR3 receptors mediate the pathological consequences of C4-OE and uncover an unexpected role of the complement in microglial processes' motility and the dynamics of microglia-neuron contacts. Indeed, microglia might be important mediators of synapse formation, which is reduced upon C4-OE.

Recent work has suggested that the effects of C4-OE on dendritic spine density are independent of CR3 and are caused by impaired trafficking of the AMPA subunit GluA1 at excitatory synapses, through an intracellular neuronal mechanism leading to a pathological decrease in synapse density.[36] Here, we employed a different approach, using electroporation at E14.5 rather than E15.5, thus targeting pyramidal neurons located deeper in layer II–III, and a different age of investigation (P15–19 vs. P21–23). The variation in methodology might contribute to the observed differences. Indeed, several studies indicate that synaptic refinement differs across cortical layers in the mammalian cortex.[37],[38] Furthermore, in SZ, dendritic spine loss affects layer III pyramidal cells but not layer V pyramidal cells.[39] These results suggest that the mechanisms of synaptic refinement might differ across pyramidal neuron populations.

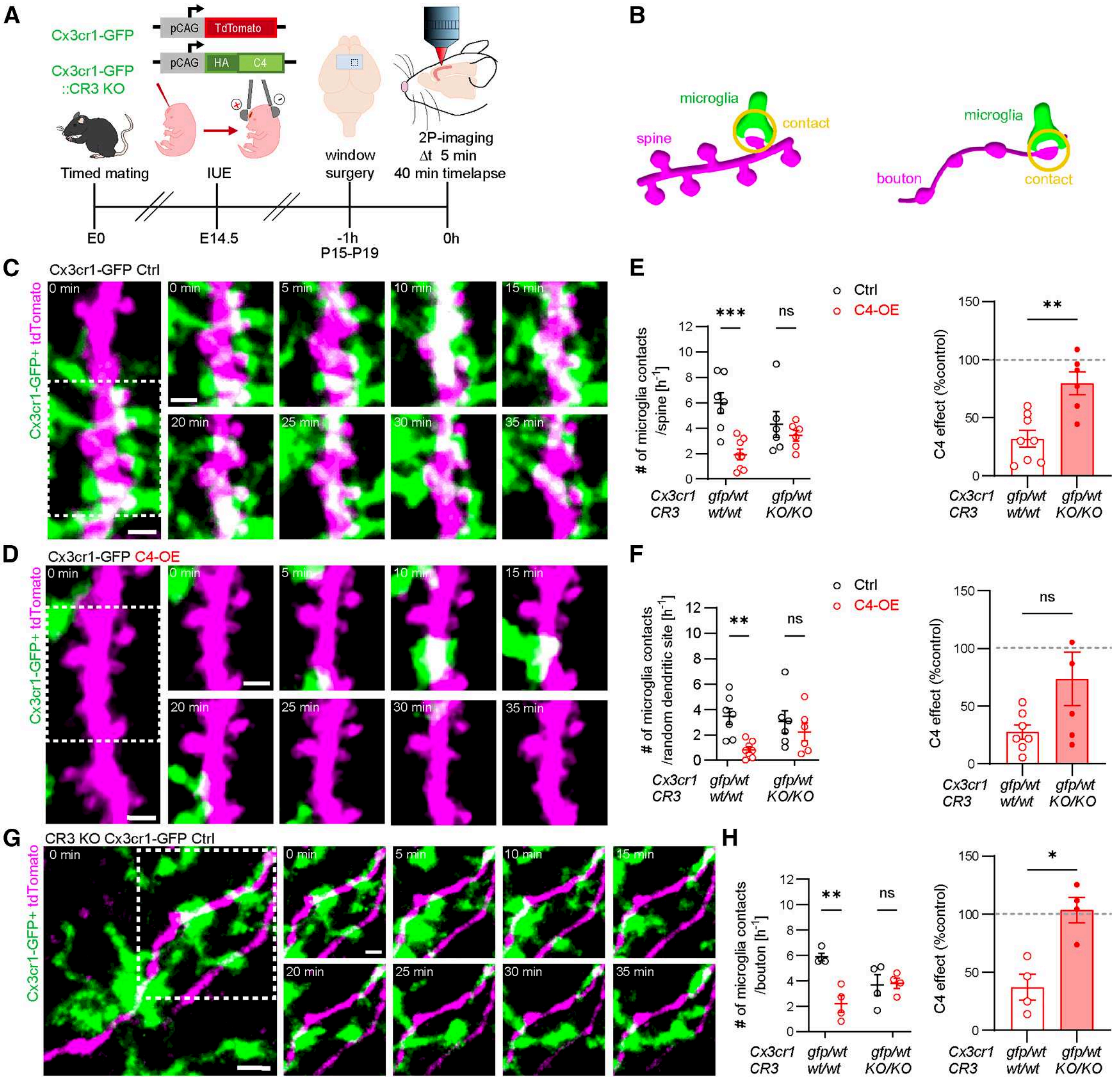

Figure 5. Decreased microglia synapse contact rate upon C4-OE is rescued by CR3 KO

(A) Schematic representation of the experimental timeline for *in vivo* imaging.

(B) Schematic representation of microglia-spine contacts and microglia-bouton contacts.

(C) Representative dendrite section of a Ctrl Cx3cr1-GFP mouse and microglia-spine contacts over 35 min. Scale bars, 2 μm.

(D) Representative dendrite section of a C4-OE Cx3cr1-GFP mouse and microglia-spine contacts. Scale bars, 2 μm.

(E) Left: dot plot showing that C4-OE significantly decreased the number of microglia contacts per spine per hour in Cx3cr1-GFP mice but not in Cx3cr1-GFP::CR3 KO mice (Dunn's test, ***p = 0.0006; Ctrl Cx3cr1-GFP: N = 7 mice; C4-OE Cx3cr1-GFP: N = 8 mice; Ctrl Cx3cr1-GFP::CR3 KO: N = 6 mice; and C4-OE Cx3cr1-GFP::CR3 KO: N = 6 mice) Right: histogram showing that the effect of C4-OE on microglia-spine contacts significantly differs across genotypes (Mann-Whitney test, **p = 0.008).

(F) Left: quantification of microglia contacts at random dendritic sites showing a significant decrease in contact rates between Ctrl Cx3cr1-GFP mice and C4-OE Cx3cr1-GFP mice (Dunn's test, **p = 0.0029; Ctrl Cx3cr1-GFP: N = 7 mice; C4-OE Cx3cr1-GFP: N = 8 mice; Ctrl Cx3cr1-GFP::CR3 KO: N = 6 mice; and C4-OE Cx3cr1-GFP::CR3 KO: N = 6 mice). Right: effect of C4-OE across genotypes (Mann-Whitney test, p = 0.075).

(G) Representative axon section of a Ctrl Cx3CR1-GFP::CR3 KO mouse and its microglia bouton contacts. Scale bars, 3 μm (left overview) and 2 μm (right, zoomed image).

(H) Left: dot plot showing significantly decreased number of microglia contacts per bouton per hour comparing Ctrl Cx3cr1-GFP mice with C4-OE Cx3cr1-GFP mice (Dunn's test, **p = 0.0028; Ctrl Cx3CR1-GFP: N = 4 mice; C4-OE Cx3CR1-GFP: N = 4 mice; Ctrl Cx3CR1-GFP::CR3KO: N = 4 mice; and C4-OE Cx3CR1-GFP::CR3KO: N = 4 mice). Right: histogram showing a significant effect of C4-OE on microglia-bouton contact rate across genotypes (Mann-Whitney test, *p = 0.029).

Data are presented as mean ± SEM error bars. ns: $p > 0.05$, not significant. Each dot represents the mean value for one mouse; 2 to 3 dendrites and 2 axons were imaged in each mouse.

Our findings present multiple lines of evidence, supporting the CR3-dependent mechanism, extending beyond mere alterations in dendritic spine density. However, our results do not exclude the possibility of a synergistic effect involving both CR3-mediated microglial changes and altered GluA1 trafficking mediating C4-OE effects.

We did not observe a significant increase in the engulfment of synaptic material by microglia as a consequence of elevated C4 expression using high-resolution imaging and 3D morphological reconstructions of microglial cells, unlike previous studies.[8,9] Different methodologies, analysis pipelines, and time points were used in these studies. Another possibility is that the spine density changes are not primarily reflecting increased spine loss as a consequence of pruning[25] or trogocytosis,[40] but decreased dendritic spine formation and/or stabilization. Consistent with this latter hypothesis, we previously reported that C4-OE decreased the formation of spines in the juvenile mouse cortex *in vivo.*[10]

Microglial dynamics and morphology changes in response to C4-OE have not been previously studied. We found that C4-OE reduced microglial motility and caused a 36% decrease in the volume surveilled by microglia, with these changes being absent in CR3 KO mice. This indicates that microglial CR3 modulates the microglial response to elevated C4 expression. Additionally, C4-OE decreased the frequencies of microglia-spine contacts by 68%, microglia-dendrite contacts by 76%, and microglia-bouton contacts by 63%. This is difficult to reconcile with the current hypothesis that iC3b, downstream of C4, selectively tags synaptic structures to be detected and engulfed by microglia, which implies that C4-OE should increase microglia-synapse contacts.

The absence of effects in mice lacking microglial CR3 suggests that reduced microglia-neuron interactions play a causal role in C4-OE-induced synaptic deficits. We propose two main hypotheses, which could operate independently or in conjunction, to account for the correlation between lower spine density and reduced microglia-spine contacts in the C4-OE model. Firstly, decreased microglia-dendritic shaft interactions may impair developmental spine formation and/or stabilization: a lack of the typical net increase in spine density between P10 and P15 may account for the comparatively lower spine density, indicating a deficit in spine formation, rather than spine elimination. This is supported by higher spine densities at P15 compared to P10 in the FC of WT mice, as reported in previous studies[30–32] and confirmed *in vivo* in Cx3cr1-GFP mice, with a 63% increase in spine density from P10/11 to P15–19 (Figure S7). The failure to reach these expected spine levels in C4-OE mice could be attributed to reduced spine formation by microglia, potentially resulting from diminished microglia-spine contacts (Figure S8). Supporting this hypothesis, several studies have shown a positive correlation between increased microglia-dendrite contacts and spine formation,[15,17] particularly during development prior to P15 in the mouse cortex.[16] In fact, live-imaging studies have consistently observed interactions between microglia and synapses that were not synaptic engulfment events,[41] supporting the notion that microglia may be more engaged in synapse formation than synapse elimination.

Secondly, microglia-synapse signaling, and thus microglial contact rate at spines, might be essential for spine stabilization and preservation of existing spines, which in turn could lead to smaller net spine density if microglia-synapse contact rate is reduced. Despite its theoretical appeal, this hypothesis has not yet been supported by experimental findings.

Additionally, neuron-dependent mechanisms may amplify the reduction in microglia-neuron contacts: reduced synaptic input and decreased spine density directly resulting from C4-OE[36] could, in turn, reduce neural network activity. Neuronal activity has been previously shown to be closely linked to microglial process motility, increasing microglia surveillance under anesthesia in the somatosensory cortex via noradrenergic signaling.[42,43] However, decreasing neuronal activity via chemogenetic silencing of glutamate release reduced microglia motility in the hippocampus.[17] Thus, reduction of network activity by C4-OE might contribute to a decrease in microglia motility and microglia surveillance, in turn resulting in less frequent microglia-synapse contacts.

Limitations of the study

In this work, sample sizes are not sufficient to support meaningful analysis of potential sex differences. Given that previous studies have reported sex-dependent effects of microglia during brain maturation,[44,45] it will be important in future studies to determine whether the effects of C4-OE on synapses and microglia are comparable between sexes,[46] and whether the absence of CR3 similarly blocks these effects in male and female mice. Another limitation of our study is that we were unable to assess the baseline role of CR3, as our experimental design did not include littermate WT controls. Consequently, we cannot verify previous findings suggesting that the absence of CR3 does not alter cortical spine density.[26] Moreover, it is important to stress that our approach based on CR3 KO mice does not exclude a potential contribution from peripheral immune cells, because outside the brain parenchyma, CR3 expression is not restricted to microglia. Although we did not detect changes in synaptic engulfment at the developmental stage examined here (P15–P19), we cannot exclude the possibility that C4-OE affected microglial synaptic engulfment at earlier stages. Nonetheless, it is worth noting that we previously reported that C4-OE does not change mEPSC frequency—a proxy for the number of functional synapses per neuron—at P9–P10 in layer 2/3 pyramidal neurons of the FC,[10] suggesting that microglia-mediated pruning does not play a major role in the effects of C4-OE during early postnatal development. Future studies should test the hypothesis that C4-OE alters microglial surveillance through reduced neuronal activity, using chemogenetic or optogenetic approaches. Such experiments could help determine whether and to what extent the observed microglial deficits arise from changes in neuronal activity or from direct CR3 receptor activation via increased iC3b binding. Future studies should also establish whether C4-OE effects are similarly mediated by CR3 in other brain regions, as our *in utero* electroporation approach restricted C4-OE to the FC.

In summary, we find that microglial CR3 receptors contribute to the detrimental effects of C4-OE on the cortical pyramidal cell synapses. C4-OE-induced changes in microglia morphology and surveillance were absent in CR3 KO mice, which, together with the selective expression of CR3 in microglia, demonstrates a key role of microglial cells in C4-OE-induced synaptic development. Together with our earlier findings showing that C4-OE diminishes spine formation, these results support a model in which elevated C4 expression reduces synapse formation by controlling microglial surveillance and, in particular, the frequency of microglia-synapse interactions in a CR3-dependent manner. Thus, our work further supports microglial roles in promoting synapse formation through process contact with dendrites during development, and that this phenomenon is regulated by CR3. This seems to contrast with the prior suggested role of CR3 in regulating synapse elimination through synaptic pruning and adds another important aspect to microglial functions that often have been associated with the so-called "synapse pruning" in cases of reduced number of synapses. Indeed, microglia can also modulate synapse densities by regulating their formation, likely via signaling mechanisms including CR3, when synapses or dendrites are contacted (Figure S8).

Reduced synapse density in the cortex of patients with SZ has been interpreted as reflecting increased synapse elimination. Our results suggest that reduced microglia-neuron interactions might impair synapse formation and thereby account for lower synapse density in SZ. This highlights the possibility for targeted treatments in SZ, aiming to modulate microglia-neuron interactions and specifically address SZ-induced synaptic pathology via iC3b-CR3 signaling. Therapeutic strategies aimed at modulating microglia would offer a fundamentally novel approach compared with current pharmacological interventions targeting neurotransmitter receptors. However, these approaches face significant challenges, including optimal timing, selective delivery of drugs crossing the blood-brain barrier to microglia, and the risk of impairing essential microglial functions with CR3 blockade, all of which require further investigation.

RESOURCE AVAILABILITY

Lead contact

Further information and requests for resources and reagents should be directed to and will be fulfilled by the lead contact, Corentin Le Magueresse (corentin.le-magueresse@inserm.fr).

Materials availability

This study did not generate new, unique reagents.

Data and code availability

- The authors declare that the results supporting the findings of this study are available within the paper, the STAR Methods section, and supplementary data files. Data reported in this paper will be shared by the lead contact upon request. The exemplary raw two-photon imaging data are available via Zenodo (https://doi.org/10.5281/zenodo.15061566).
- This paper does not report original code. Full details regarding the microglia motility analysis can be found in an open-access publication (https://joss.theoj.org/papers/10.21105/joss.09267). The corresponding source code, documentation, tutorials, and issue tracking are hosted at https://github.com/FabrizioMusacchio/motila.
- Any additional information required to reanalyze the data reported in this paper is available from the lead contact upon request.

ACKNOWLEDGMENTS

The authors wish to thank the Cell and Tissue Imaging Facility at the Institut du Fer à Moulin (Theano Eirinopoulou and Mythili Savariradjane) and the Light Microscopy Facility at DZNE Bonn (Hans Fried and Severin Filser), as well as the Animal Research Facilities at DZNE Bonn and IFM. We thank Julia Steffen and Andrea Baral for technical assistance and Paolo Salomoni, Anne Roumier, and Jean-Antoine Girault for valuable comments on the manuscript. M.D. was a recipient of PhD fellowships from the Doctoral School "Brain Cognition and Behavior" of Sorbonne University and the Fondation pour la Recherche Médicale/Venite Cantemus. This work was supported by DZNE (M.F.); the University of Latvia (B.J.); Inserm (C.L.M.); and grants from ANR to C.L.M. (ANR-24-CE16-5833-01), from the Fondation de France to C.L.M. (FDF#00112562), and ERA-Net NEURON to C.L.M. (ANR-18-NEUR-008-02), M.F. (BMBF 01EW1905), and B.J. (VIAA 1.1.1.5/ERANET/20/01). C.L.M. is a member of the DIM C-BRAINS funded by the Conseil Régional d'Ile-de-France, a member of the Institut du Cerveau de l'Enfant (ANR-23-IAHU-001), and is supported by the Fédération pour la Recherche sur le Cerveau. The work was supported by the European Union ERC-CoG (MicroSynCom 865618). M.F., N.G., F.F., and F.M. received funding from the German Research Foundation DFG (SFB1089 C01, B06, and SPP2395), and M.F. is a member of the DFG excellence cluster ImmunoSensation2. This work was also supported by the iBehave network to M.F. and S.P. (funded by the Ministry of Culture and Science of the State of North Rhine-Westphalia; the funders had no role in study design, data collection, and interpretation, or the decision to submit the work for publication).

AUTHOR CONTRIBUTIONS

N.G. and N.N.-R. carried out the experiments, performed surgeries, collected data, analyzed the data, designed the figures, and wrote the manuscript. M.D. carried out and analyzed the electrophysiological measurements. K.J. performed biochemical analysis. F.F. and S.P. contributed to surgical procedures. F.M. analyzed data. M.M. performed clustering analysis. H.A. contributed to confocal imaging and Imaris reconstruction. S.C.-D. supported the experimental work. M.F. and C.L.M. supervised the project. B.J., M.F., and C.L.M. provided resources and technical expertise, conceptualized the experiments, and wrote the manuscript.

DECLARATION OF INTERESTS

The authors declare no competing interests.

STAR★METHODS

Detailed methods are provided in the online version of this paper and include the following:

- KEY RESOURCES TABLE
- EXPERIMENTAL MODEL AND STUDY PARTICIPANT DETAILS
- METHOD DETAILS
  - DNA plasmid constructs
  - In utero electroporation
  - Acute slice preparation
  - Electrophysiology recordings
  - Miniature EPSCs and miniature IPSCs
  - AMPA/NMDA ratio
  - Histology and immunohistochemistry
  - Confocal microscopy of fixed brain tissue
  - Reconstruction of synaptic inclusions within microglial cells
  - Surveilled volume analysis
  - Reconstruction of dendritic fragments
  - Cluster analysis
  - Western immunoblotting
  - Microglial cell density
  - Cranial window surgery
  - *In vivo* two-photon imaging
- QUANTIFICATION AND STATISTICAL ANALYSIS
  - Microglial motility analysis
  - Analysis of microglia-synapse and microglia-dendrite contacts
  - Statistics

SUPPLEMENTAL INFORMATION

Supplemental information can be found online at https://doi.org/10.1016/j.celrep.2026.117161.

Received: July 25, 2025
Revised: January 26, 2026
Accepted: March 3, 2026

REFERENCES

1. McCutcheon, R.A., Reis Marques, T., and Howes, O.D. (2020). Schizophrenia-An Overview. JAMA Psychiatry *77*, 201–210. https://doi.org/10.1001/jamapsychiatry.2019.3360.
2. Glantz, L.A., and Lewis, D.A. (2000). Decreased dendritic spine density on prefrontal cortical pyramidal neurons in schizophrenia. Arch. Gen. Psychiatry *57*, 65–73.
3. Kuperberg, G.R., Broome, M.R., McGuire, P.K., David, A.S., Eddy, M., Ozawa, F., Goff, D., West, W.C., Williams, S.C.R., van der Kouwe, A.J.W., et al. (2003). Regionally localized thinning of the cerebral cortex in schizophrenia. Arch. Gen. Psychiatry *60*, 878–888. https://doi.org/10.1001/archpsyc.60.9.878.
4. Onwordi, E.C., Halff, E.F., Whitehurst, T., Mansur, A., Cotel, M.C., Wells, L., Creeney, H., Bonsall, D., Rogdaki, M., Shatalina, E., et al. (2020). Synaptic density marker SV2A is reduced in schizophrenia patients and unaffected by antipsychotics in rats. Nat. Commun. *11*, 246. https://doi.org/10.1038/s41467-019-14122-0.
5. Trubetskoy, V., Pardiñas, A.F., Qi, T., Panagiotaropoulou, G., Awasthi, S., Bigdeli, T.B., Bryois, J., Chen, C.Y., Dennison, C.A., Hall, L.S., et al. (2022). Mapping genomic loci implicates genes and synaptic biology in schizophrenia. Nature *604*, 502–508. https://doi.org/10.1038/s41586-022-04434-5.
6. Sekar, A., Bialas, A.R., de Rivera, H., Davis, A., Hammond, T.R., Kamitaki, N., Tooley, K., Presumey, J., Baum, M., Van Doren, V., et al. (2016). Schizophrenia risk from complex variation of complement component 4. Nature *530*, 177–183. https://doi.org/10.1038/nature16549.
7. Sellgren, C.M., Gracias, J., Watmuff, B., Biag, J.D., Thanos, J.M., Whittredge, P.B., Fu, T., Worringer, K., Brown, H.E., Wang, J., et al. (2019). Increased synapse elimination by microglia in schizophrenia patient-derived models of synaptic pruning. Nat. Neurosci. *22*, 374–385. https://doi.org/10.1038/s41593-018-0334-7.
8. Comer, A.L., Jinadasa, T., Sriram, B., Phadke, R.A., Kretsge, L.N., Nguyen, T.P.H., Antognetti, G., Gilbert, J.P., Lee, J., Newmark, E.R., et al. (2020). Increased expression of schizophrenia-associated gene C4 leads to hypoconnectivity of prefrontal cortex and reduced social interaction. PLoS Biol. *18*, e3000604. https://doi.org/10.1371/journal.pbio.3000604.
9. Yilmaz, M., Yalcin, E., Presumey, J., Aw, E., Ma, M., Whelan, C.W., Stevens, B., McCarroll, S.A., and Carroll, M.C. (2021). Overexpression of schizophrenia susceptibility factor human complement C4A promotes excessive synaptic loss and behavioral changes in mice. Nat. Neurosci. *24*, 214–224. https://doi.org/10.1038/s41593-020-00763-8.
10. Druart, M., Nosten-Bertrand, M., Poll, S., Crux, S., Nebeling, F., Delhaye, C., Dubois, Y., Mittag, M., Leboyer, M., Tamouza, R., et al. (2021). Elevated expression of complement C4 in the mouse prefrontal cortex causes schizophrenia-associated phenotypes. Mol. Psychiatry *26*, 3489–3501. https://doi.org/10.1038/s41380-021-01081-6.
11. Presumey, J., Bialas, A.R., and Carroll, M.C. (2017). Complement System in Neural Synapse Elimination in Development and Disease. Adv. Immunol. *135*, 53–79. https://doi.org/10.1016/bs.ai.2017.06.004.
12. Tremblay, M.È., Lowery, R.L., and Majewska, A.K. (2010). Microglial interactions with synapses are modulated by visual experience. PLoS Biol. *8*, e1000527. https://doi.org/10.1371/journal.pbio.1000527.
13. Sipe, G.O., Lowery, R.L., Tremblay, M.È., Kelly, E.A., Lamantia, C.E., and Majewska, A.K. (2016). Microglial P2Y12 is necessary for synaptic plasticity in mouse visual cortex. Nat. Commun. *7*, 10905. https://doi.org/10.1038/ncomms10905.
14. Choudhury, M.E., Miyanishi, K., Takeda, H., Islam, A., Matsuoka, N., Kubo, M., Matsumoto, S., Kunieda, T., Nomoto, M., Yano, H., and Tanaka, J. (2020). Phagocytic elimination of synapses by microglia during sleep. Glia *68*, 44–59. https://doi.org/10.1002/glia.23698.
15. Parkhurst, C.N., Yang, G., Ninan, I., Savas, J.N., Yates, J.R., 3rd, Lafaille, J.J., Hempstead, B.L., Littman, D.R., and Gan, W.B. (2013). Microglia promote learning-dependent synapse formation through brain-derived neurotrophic factor. Cell *155*, 1596–1609. https://doi.org/10.1016/j.cell.2013.11.030.
16. Miyamoto, A., Wake, H., Ishikawa, A.W., Eto, K., Shibata, K., Murakoshi, H., Koizumi, S., Moorhouse, A.J., Yoshimura, Y., and Nabekura, J. (2016). Microglia contact induces synapse formation in developing somatosensory cortex. Nat. Commun. *7*, 12540. https://doi.org/10.1038/ncomms12540.
17. Nebeling, F.C., Poll, S., Justus, L.C., Steffen, J., Keppler, K., Mittag, M., and Fuhrmann, M. (2023). Microglial motility is modulated by neuronal activity and correlates with dendritic spine plasticity in the hippocampus of awake mice. eLife *12*, e83176. https://doi.org/10.7554/eLife.83176.
18. Roumier, A., Pascual, O., Béchade, C., Wakselman, S., Poncer, J.C., Réal, E., Triller, A., and Bessis, A. (2008). Prenatal activation of microglia induces delayed impairment of glutamatergic synaptic function. PLoS One *3*, e2595. https://doi.org/10.1371/journal.pone.0002595.
19. Basilico, B., Pagani, F., Grimaldi, A., Cortese, B., Di Angelantonio, S., Weinhard, L., Gross, C., Limatola, C., Maggi, L., and Ragozzino, D. (2019). Microglia shape presynaptic properties at developing glutamatergic synapses. Glia *67*, 53–67. https://doi.org/10.1002/glia.23508.
20. Basilico, B., Ferrucci, L., Ratano, P., Golia, M.T., Grimaldi, A., Rosito, M., Ferretti, V., Reverte, I., Sanchini, C., Marrone, M.C., et al. (2022). Microglia control glutamatergic synapses in the adult mouse hippocampus. Glia *70*, 173–195. https://doi.org/10.1002/glia.24101.
21. Stevens, B., Allen, N.J., Vazquez, L.E., Howell, G.R., Christopherson, K.S., Nouri, N., Micheva, K.D., Mehalow, A.K., Huberman, A.D., Stafford, B., et al. (2007). The classical complement cascade mediates CNS synapse elimination. Cell *131*, 1164–1178. https://doi.org/10.1016/j.cell.2007.10.036.
22. Druart, M., and Le Magueresse, C. (2019). Emerging Roles of Complement in Psychiatric Disorders. Front. Psychiatry *10*, 573. https://doi.org/10.3389/fpsyt.2019.00573.
23. Perry, V.H., Hume, D.A., and Gordon, S. (1985). Immunohistochemical localization of macrophages and microglia in the adult and developing mouse brain. Neuroscience *15*, 313–326. https://doi.org/10.1016/0306-4522(85)90215-5.
24. Akiyama, H., and McGeer, P.L. (1990). Brain microglia constitutively express beta-2 integrins. J. Neuroimmunol. *30*, 81–93. https://doi.org/10.1016/0165-5728(90)90055-r.
25. Schafer, D.P., Lehrman, E.K., Kautzman, A.G., Koyama, R., Mardinly, A.R., Yamasaki, R., Ransohoff, R.M., Greenberg, M.E., Barres, B.A., and Stevens, B. (2012). Microglia sculpt postnatal neural circuits in an activity and complement-dependent manner. Neuron *74*, 691–705. https://doi.org/10.1016/j.neuron.2012.03.026.
26. Deivasigamani, S., Miteva, M.T., Natale, S., Gutierrez-Barragan, D., Basilico, B., Di Angelantonio, S., Weinhard, L., Molotkov, D., Deb, S., Pape, C., et al. (2023). Microglia complement signaling promotes neuronal elimination and normal brain functional connectivity. Cereb. Cortex *33*, 10750–10760. https://doi.org/10.1093/cercor/bhad313.
27. Holtmaat, A.J.G.D., Trachtenberg, J.T., Wilbrecht, L., Shepherd, G.M., Zhang, X., Knott, G.W., and Svoboda, K. (2005). Transient and persistent dendritic spines in the neocortex in vivo. Neuron *45*, 279–291. https://doi.org/10.1016/j.neuron.2005.01.003.

28. Zuo, Y., Lin, A., Chang, P., and Gan, W.B. (2005). Development of long-term dendritic spine stability in diverse regions of cerebral cortex. Neuron *46*, 181–189. https://doi.org/10.1016/j.neuron.2005.04.001.

29. Cruz-Martín, A., Crespo, M., and Portera-Cailliau, C. (2010). Delayed stabilization of dendritic spines in fragile X mice. J. Neurosci. *30*, 7793–7803. https://doi.org/10.1523/JNEUROSCI.0577-10.2010.

30. Balu, D.T. (2016). The NMDA Receptor and Schizophrenia: From Pathophysiology to Treatment. Adv. Pharmacol. *76*, 351–382. https://doi.org/10.1016/bs.apha.2016.01.006.

31. Hammond, T.R., Dufort, C., Dissing-Olesen, L., Giera, S., Young, A., Wysoker, A., Walker, A.J., Gergits, F., Segel, M., Nemesh, J., et al. (2019). Single-Cell RNA Sequencing of Microglia throughout the Mouse Lifespan and in the Injured Brain Reveals Complex Cell-State Changes. Immunity *50*, 253–271.e6. https://doi.org/10.1016/j.immuni.2018.11.004.

32. Franco, R., and Fernández-Suárez, D. (2015). Alternatively activated microglia and macrophages in the central nervous system. Prog. Neurobiol. *131*, 65–86. https://doi.org/10.1016/j.pneurobio.2015.05.003.

33. Lehnardt, S. (2010). Innate immunity and neuroinflammation in the CNS: the role of microglia in Toll-like receptor-mediated neuronal injury. Glia *58*, 253–263. https://doi.org/10.1002/glia.20928.

34. Nguyen, L.K., Kholodenko, B.N., and von Kriegsheim, A. (2018). Rac1 and RhoA: Networks, loops and bistability. Small GTPases *9*, 316–321. https://doi.org/10.1080/21541248.2016.1224399.

35. Arnold, T.R., Stephenson, R.E., and Miller, A.L. (2017). Rho GTPases and actomyosin: Partners in regulating epithelial cell-cell junction structure and function. Exp. Cell Res. *358*, 20–30. https://doi.org/10.1016/j.yexcr.2017.03.053.

36. Phadke, R.A., Brack, A., Fournier, L.A., Kruzich, E., Sha, M., Picard, I., Johnson, C., Stroumbakis, D., Salgado, M., Yeung, C., et al. (2025). The schizophrenia risk gene C4 induces pathological synaptic loss by impairing AMPAR trafficking. Mol. Psychiatry *30*, 796–809. https://doi.org/10.1038/s41380-024-02701-7.

37. Bourgeois, J.P., and Rakic, P. (1993). Changes of synaptic density in the primary visual cortex of the macaque monkey from fetal to adult stage. J. Neurosci. *13*, 2801–2820.

38. Petanjek, Z., Judaš, M., Šimic, G., Rasin, M.R., Uylings, H.B.M., Rakic, P., and Kostovic, I. (2011). Extraordinary neoteny of synaptic spines in the human prefrontal cortex. Proc. Natl. Acad. Sci. USA *108*, 13281–13286. https://doi.org/10.1073/pnas.1105108108.

39. Kolluri, N., Sun, Z., Sampson, A.R., and Lewis, D.A. (2005). Lamina-specific reductions in dendritic spine density in the prefrontal cortex of subjects with schizophrenia. Am. J. Psychiatry *162*, 1200–1202. https://doi.org/10.1176/appi.ajp.162.6.1200.

40. Weinhard, L., di Bartolomei, G., Bolasco, G., Machado, P., Schieber, N.L., Neniskyte, U., Exiga, M., Vadisiute, A., Raggioli, A., Schertel, A., et al. (2018). Microglia remodel synapses by presynaptic trogocytosis and spine head filopodia induction. Nat. Commun. *9*, 1228. https://doi.org/10.1038/s41467-018-03566-5.

41. Eyo, U., and Molofsky, A.V. (2023). Defining microglial-synapse interactions. Science *381*, 1155–1156. https://doi.org/10.1126/science.adh7906.

42. Liu, Y.U., Ying, Y., Li, Y., Eyo, U.B., Chen, T., Zheng, J., Umpierre, A.D., Zhu, J., Bosco, D.B., Dong, H., and Wu, L.J. (2019). Neuronal network activity controls microglial process surveillance in awake mice via norepinephrine signaling. Nat. Neurosci. *22*, 1771–1781. https://doi.org/10.1038/s41593-019-0511-3.

43. Stowell, R.D., Sipe, G.O., Dawes, R.P., Batchelor, H.N., Lordy, K.A., Whitelaw, B.S., Stoessel, M.B., Bidlack, J.M., Brown, E., Sur, M., and Majewska, A.K. (2019). Noradrenergic signaling in the wakeful state inhibits microglial surveillance and synaptic plasticity in the mouse visual cortex. Nat. Neurosci. *22*, 1782–1792. https://doi.org/10.1038/s41593-019-0514-0.

44. VanRyzin, J.W., Marquardt, A.E., Pickett, L.A., and McCarthy, M.M. (2020). Microglia and sexual differentiation of the developing brain: A focus on extrinsic factors. Glia *68*, 1100–1113. https://doi.org/10.1002/glia.23740.

45. Bordt, E.A., Ceasrine, A.M., and Bilbo, S.D. (2020). Microglia and sexual differentiation of the developing brain: A focus on ontogeny and intrinsic factors. Glia *68*, 1085–1099. https://doi.org/10.1002/glia.23753.

46. Fournier, L.A., Phadke, R.A., Salgado, M., Brack, A., Nocon, J.C., Bolshakova, S., Grant, J.R., Padró Luna, N.M., Sen, K., and Cruz-Martín, A. (2024). Overexpression of the schizophrenia risk gene C4 in PV cells drives sex-dependent behavioral deficits and circuit dysfunction. iScience *27*, 110800. https://doi.org/10.1016/j.isci.2024.110800.

47. Coxon, A., Rieu, P., Barkalow, F.J., Askari, S., Sharpe, A.H., von Andrian, U.H., Arnaout, M.A., and Mayadas, T.N. (1996). A novel role for the beta 2 integrin CD11b/CD18 in neutrophil apoptosis: a homeostatic mechanism in inflammation. Immunity *5*, 653–666. https://doi.org/10.1016/s1074-7613(00)80278-2.

48. Jung, S., Aliberti, J., Graemmel, P., Sunshine, M.J., Kreutzberg, G.W., Sher, A., and Littman, D.R. (2000). Analysis of fractalkine receptor CX(3)CR1 function by targeted deletion and green fluorescent protein reporter gene insertion. Mol. Cell Biol. *20*, 4106–4114.

49. Matsuda, T., and Cepko, C.L. (2004). Electroporation and RNA interference in the rodent retina in vivo and in vitro. Proc. Natl. Acad. Sci. USA *101*, 16–22. https://doi.org/10.1073/pnas.2235688100.

50. Rothman, J.S., and Silver, R.A. (2018). NeuroMatic: An Integrated Open-Source Software Toolkit for Acquisition, Analysis and Simulation of Electrophysiological Data. Front. Neuroinform. *12*, 14. https://doi.org/10.3389/fninf.2018.00014.

51. Pfeiffer, T., Poll, S., Bancelin, S., Angibaud, J., Inavalli, V.K., Keppler, K., Mittag, M., Fuhrmann, M., and Nägerl, U.V. (2018). Chronic 2P-STED imaging reveals high turnover of dendritic spines in the hippocampus in vivo. eLife *7*, e34700. https://doi.org/10.7554/eLife.34700.

52. Fuhrmann, M., Bittner, T., Jung, C.K.E., Burgold, S., Page, R.M., Mitteregger, G., Haass, C., LaFerla, F.M., Kretzschmar, H., and Herms, J. (2010). Microglial Cx3cr1 knockout prevents neuron loss in a mouse model of Alzheimer's disease. Nat. Neurosci. *13*, 411–413. https://doi.org/10.1038/nn.2511.

53. Guizar-Sicairos, M., Thurman, S.T., and Fienup, J.R. (2008). Efficient subpixel image registration algorithms. Opt. Lett. *33*, 156–158. https://doi.org/10.1364/ol.33.000156.

54. van der Walt, S., Schönberger, J.L., Nunez-Iglesias, J., Boulogne, F., Warner, J.D., Yager, N., Gouillart, E., and Yu, T.; scikit-image contributors (2014). scikit-image: image processing in Python. PeerJ *2*, e453. https://doi.org/10.7717/peerj.453.

55. Otsu, N. (1979). A Threshold Selection Method from Gray-Level Histograms. IEEE Trans. Syst. Man Cybern. *9*, 62–66. https://doi.org/10.1109/TSMC.1979.4310076.

56. Pizer, S.M., Amburn, E.P., Austin, J.D., Cromartie, R., Geselowitz, A., Greer, T., ter Haar Romeny, B., Zimmerman, J.B., and Zuiderveld, K. (1987). Adaptive histogram equalization and its variations. Comput. Vis. Graph Image Process *39*, 355–368. https://doi.org/10.1016/S0734-189X(87)80186-X.

57. Gu, L., Kleiber, S., Schmid, L., Nebeling, F., Chamoun, M., Steffen, J., Wagner, J., and Fuhrmann, M. (2014). Long-term in vivo imaging of dendritic spines in the hippocampus reveals structural plasticity. J. Neurosci. *34*, 13948–13953. https://doi.org/10.1523/JNEUROSCI.1464-14.2014.

STAR★METHODS

KEY RESOURCES TABLE

REAGENT or RESOURCE	SOURCE	IDENTIFIER
Antibodies		
Rabbit anti-Iba1	Wako	019–19741, RRID: AB_839504
Rabbit anti-Iba1	Synaptic Systems	HS-234-013; RRID:AB_2661873
Rabbit anti-synaptophysin	Abcam	AB32127; RRID: AB_2286949
Rat anti-CD68	Acris	AM33123SU-N; RRID: N/A
Chicken-*anti*-Homer1	Synaptic systems	16006; RRID: N/A
Chicken anti-GFP	Abcam	AB13970, RRID: AB_300798
Mouse-*anti*-Bassoon	Abcam	AB82958, RRID: AB1860018
Mouse-anti_Rac1-GTP	New east Bio	26903; RRID:AB_1961793
Mouse-anti RhoA-GTP	New east Bio	26904; RRID:AB_1961799
Rat anti-HA	Sigma	AB_390919; RRID:AB_390919
Goat anti-rabbit Alexa Fluor 488	Life Technologies	A11034; RRID:AB_2576217
Goat anti-rat Alexa Fluor 488	Invitrogen	AB_2534074; RRID:AB_2534074
Goat-*anti*-rat Alexa Fluor 405	Invitrogen	A48261; RRID:AB_2890550
Goat-*anti*-chicken Alexa Fluor 647	Invitrogen	A32933; RRID:AB_2762845
Goat-*anti*-mouse Alexa Fluor 647	Invitrogen	A21235; RRID:AB_2535804
Goat-*anti*-rabbit Alexa Fluor 647	Invitrogen	A21244; RRID:AB_2535812
Iba1 monoclonal antibody [EPR16588]	Abcam	AB_2636859; RRID:AB_2636859
TLR4 monoclonal antibody	Santa Cruz Biotecnology	AB_10611320; RRID:AB_10611320
mCSF recombinant antibody	Abcam	AB_2892678; RRID:AB_2892678
Osteopontin polyclonal antibody	Abcam	AB_1524127; RRID:AB_1524127
Actin-beta monoclonal antibody	Sigma-Aldrich	AB_476697; RRID:AB_476697
Actin-beta monoclonal antibody	LiCor	AB_1850027; RRID:AB_1850027
Chemicals, Peptides and recombinant proteins		
Plasmid Mega Kit	Qiagen	Cat#12181
pCAG-C4HA	C. Le Magueresse team	N/A
pCAG-tdTomato	C. Le Magueresse team	N/A
Experimental Models: Mouse strains		
C57Bl6/J	Janvier Labs	C57BL/6JRj
CR3 KO	The Jackson laboratory #3991	B6.129S4-Itgam^{tm1My}d/J
Cx3cr1^{gfp}	The Jackson laboratory #5582	B6.129P2(Cg)-Cx3cr1^{tm1Litt}/J
Software and algorithms		
GraphPad Prism	Dotmatics	https://www.graphpad.com/
Adobe Illustrator	Adobe Systems Inc	https://www.adobe.com/de/products/illustrator.html
ImageJ	NIH	https://imagej.nih.gov/ij/
Imaris Studio	Oxford instruments Bitplane	http://www.bitplane.com/imaris
MiniAnalysis	SynaptoSoft	N/A
Zen Blue & Black	Carl Zeiss AG	https://www.zeiss.com/microscopy/de/produkte/software/zeiss-zen.html
Igor Pro	WaveMetrics	https://www.wavemetrics.com/products/igorpro
NeuroMatic	JS Rothman and RA Silver, UCL	http://www.neuromatic.thinkrandom.com/
Python	Python Software Foundation	https://www.python.org/

(*Continued on next page*)

Continued

REAGENT or RESOURCE	SOURCE	IDENTIFIER
PatchMaster	HEKA	http://www.heka.com/products/products_main.html
Python pipeline for microglia motility analysis	M. Fuhrmann team	https://joss.theoj.org/papers/10.21105/joss.09267
Research Randomizer (Version 4.0)	G.C. Urbaniak and S. Plous (2013)	https://www.randomizer.org/

EXPERIMENTAL MODEL AND STUDY PARTICIPANT DETAILS

All animal experiments were performed according to guidelines of the European Community for the use of animals in research and were approved by the local ethical committees (C2EA-05 in France; LANUV NRW in Germany). Experiments were conducted on mice subjected to *in utero* electroporation at E14.5, kept in specific pathogen-free facilities. Mice were group-housed by sex (2–5 per cage), and kept under a 12h light/dark cycle at 22 ± 2°C. Bedding consisted of autoclaved wood shavings to 1 cm depth, and was changed once every two weeks. All cages contained nesting material (sterilized shredded paper) and enrichment material consisting of a translucent plastic hut. Food and water were available *ad libitum*. Daily health checks monitored the mice's general appearance along with their food and water intake. We used B6.129S4-*Itgam*^{tm1Myd}/J mice (Jackson laboratory, RRID: 003991) which lack the gene encoding integrin αM-CD11B, an obligatory subunit of the complement CR3 receptor[47]; referred to as CR3 KO mice throughout the manuscript. CR3 KO mice were regularly backcrossed (for >10 generations prior to the beginning of the experimental work) on a C57Bl/6J background. *In utero* electroporations were performed on homozygous CR3 KO females which had been bred with homozygous CR3 KO males, or wild-type (WT) C57Bl/6J controls. Cx3cr1-GFP knock-in mice carry the international name: B6.129P-CX3CR1tm1Litt/J (Jackson laboratory, RRID: 005582). The *Gfp* gene is introduced as a knock-in into the allele of the *Cx3cr1* gene (chemokine C-X3-C motif receptor 1),[48] leading to GFP expression in macrophages and thus in microglia in the brain. To obtain Cx3cr1$^{gfp/wt}$::CR3$^{KO/KO}$ progeny for *in utero* electroporations, Cx3cr1$^{gfp/gfp}$::CR3$^{KO/KO}$ were bred to Cx3cr1$^{wt/wt}$::CR3$^{KO/KO}$ mice. Equivalent numbers of males and females were included and randomly assigned for electrophysiology, immunohistochemistry and imaging experiments.

METHOD DETAILS

DNA plasmid constructs

Plasmids constructs (pCAG-C4HA and pCAG-tdTomato) were previously generated in our team.[10] The cDNA of murine C4b was obtained by reverse transcription PCR of total RNA from brains of adult 129S1/SvImJ mice. An HA tag sequence was inserted at the 5′ end of the *C4b* cDNA sequence to allow identification of C4-overexpressing cells. pCAG-tdTomato expression vector design was based on pCAG-mGFP which was a gift from Dr. C Cepko[49] (Addgene plasmid #14757). mGFP was replaced by TdTomato in the pCAG backbone. Subcloning of *C4b* and *tdTomato* sequences were done using InFusi (Clonetech) and DNA were purified with Nucleospin kit (Macherey-Nagel). Constructs were verified by sequencing.

In utero electroporation

Pregnant WT and CR3 KO mice, or Cx3cr1-GFP and Cx3cr1-GFP::CR3 KO mice, were injected at E14.5 with Meloxicam (5 mg/kg s.c. 30 min before surgical procedure) and later anesthetized with isoflurane 4%. Surgery was performed under isoflurane 2% on a heated blanket and breathing was carefully monitored during all the procedure. A midline laparotomy was performed, and the uterine horns were exposed and moisturized with sterile NaCl 0.9%. 0.5 to 1μL of a solution containing pCAG-C4HA vector (0.8μg/μL) together with pCAG-tdTomato vector (0.4 μg/μL) (molar ratio 4:1) prepared in NaCl 0.9% were injected in the lateral ventricles with a glass micropipette made from a microcapillary tube (#5-000-1001-x10, Drummond Scientific). For the control condition, we injected a solution containing pCAG-tdTomato (0.8 μg/μL) only. The injected plasmid solution contained Fast Green (0.1%) to monitor the injection. The embryo's head in the uterus was held between the tweezer-type electrode consisting of two 5 mm diameter disc electrodes (CUY650P5, Nepagene). The cathode was placed above the olfactory bulbs and the anode was placed at the back of the head. Electrical pulses (50 V; 50 ms) were applied five times at intervals of 950 ms with an electroporator (CUY21 Edit, Nepagene). The uterine horns were placed back into the abdominal cavity which was then filled up with sterile NaCl 0.9%. The abdominal muscle and skin were sutured separately. Mice were left on a heated plate for recovery and were subsequently returned to their home cage. Sutures were monitored daily until birth. Successful plasmid electroporation was confirmed shortly after birth (P1-P2) using magnifying goggles (FS/ULS-02 G2, Biological laboratory equipment maintenance and service Ltd.) that allowed the visualization of fluorescence through the intact skin and skull, and also confirmed *postmortem* on brain slices from each experimental animal. The surgical procedure was performed in alternance for the four different conditions (Ctrl WT; C4-OE WT; Ctrl CR3 KO; C4-OE CR3 KO) to avoid experimental bias.

Acute slice preparation

250 μm-thick sagittal slices were prepared from brains of the six different experimental groups from juvenile mice aged P15-P18. Mice were deeply anesthetized with sodium pentobarbital (150 mg/Kg) followed by brains' dissection which were immediately transferred to a plate filled with artificial cerebrospinal fluid (ACSF) containing the following (in mM): 125 NaCl, 2.5 KCl, 25 glucose, 25 $NaHCO_3$, 1.25 NaH_2PO4, 2 $CaCl_2$ and 1 $MgCl_2$, continuously bubbled with 95% O_2-5% CO_2. Acute sagittal slices were cut in the same ice-cold solution using a vibroslicer (HM 650 V, Microm). Slices were incubated in ACSF at 32°C for 20 min and then at room temperature (20°–25°C). For patch-clamp recordings, slices were transferred to the recording chamber where they were continuously perfused with ACSF (30°–32°C) buffered by continuous bubbling with 95% O_2-5% CO_2.

Electrophysiology recordings

Whole-cell voltage-clamp recordings were performed in layer II-III pyramidal cells of the frontal cortex (FC). Recorded pyramidal cells all expressed tdTomato. Stimulus delivery and data acquisition were performed using Patchmaster software (Multichannel systems). Signals were acquired with an EPC10-USB amplifier (Multichannel systems), sampled at 20 kHz and filtered at 4 kHz. Offline analysis was performed using Clampfit (Molecular Devices), IgorPro (Wavemetrics) and the Neuromatic toolkit for IgorPro.[50] For the study of miniature post-synaptic currents, recordings were filtered offline at 2 kHz and analyzed using MiniAnalysis (Synaptosoft). Patch-clamp pipettes (5–6 Mohm resistance) were prepared from borosilicate glass (BF150-86-10, Harvard Apparatus) using a DMZ pipette puller (Zeitz). For voltage-clamp experiments the following intracellular solution was used (in mM): 120 Cs-methane sulfonate, 10 CsCl, 10 HEPES, 10 Phosphocreatinine, 0.2 EGTA, 8 NaCl, 2 ATP-Mg, 3 QX 314 (pH 7.25, adjusted with CsOH). To record miniature inhibitory post-synaptic currents (mIPSCs) we used a high-chloride intracellular solution containing (in mM): 60 Cs methane sulfonate, 70 CsCl, 10 HEPES, 10 Phosphocreatinine, 0.2 EGTA, 8 NaCl, 2 ATP-Mg (pH 7.25, adjusted with CsOH).

Miniature EPSCs and miniature IPSCs

Miniature excitatory postsynaptic currents (mEPSCs) were recorded at a holding potential of −65mV in the presence of Tetrodotoxin (TTX, 0.5 μM) and Gabazine (SR 95531, 10 μM). 100 s were analyzed for each recording. mIPSCs were recorded at a holding potential of −65mV in the presence of TTX (0.5 μM), CNQX (10 μM) and D-APV (50 μM). 100 s were analyzed for each recording. Data analysis was performed under blinded conditions.

AMPA/NMDA ratio

To measure the AMPA/NMDA ratio, EPSCs were evoked with a monopolar electrode connected to a constant current stimulator (Iso-Flex, A.M.P.I.) positioned in layer III, around 100-150μm away from the recorded neuron. Between 12 and 15 consecutive sweeps were acquired at a frequency of 0.1 Hz and averaged at each holding potential. The AMPA/NMDA ratio was recorded in the presence of GABAzine (10μM). The AMPA current (I_{AMPA}) was measured as the peak amplitude of the current response at a holding potential of −65mV. The NMDA current (I_{NMDA}) was measured at a holding potential of +55mV, 50ms after stimulation, when AMPAR-mediated currents have receded due to the fast deactivation kinetics of AMPARs. The ratio was calculated as I_{AMPA}/I_{NMDA}. For each recorded neuron, the decay time constant of NMDA currents was determined by fitting a single exponential function to the decay phase of the average NMDA current from 50 ms to 250 ms after stimulation. Data analysis was performed under blinded conditions.

Histology and immunohistochemistry

Mice aged P15-P19 were anesthetized with pentobarbital (150 mg/Kg) and intracardially perfused with NaCl 0.9% followed by 4% buffered formaldehyde (Histofix, Roti). The brains were dissected and fixed overnight in 4% Histofix. 100μm sagittal sections were cut using a vibratome (VT1200S, Leica). For immunohistochemistry, free-floating sections were permeabilized and blocked in 0.2% Triton-PBS, 3% BSA-PBS for 60min before incubation with first antibody in 0.2% Triton, 3% BSA-PBS overnight at 4°C. After three consecutive rinses with PBS, sections were incubated with the secondary antibody in PBS for 2h, washed again in PBS and then mounted using Fluoromount G (Invitrogen). Primary antibodies were Rat anti-HA (1:300, Sigma #AB390919), Rabbit anti-Iba1 (1:500 Synaptic Systems #HS-234-013 for microglia morphology/density) and Rabbit anti-Iba1 (1:1000, Wako #019–19741) Rat anti-CD68 (1:400, Acris #SM1550P), Chicken anti-Homer1 (1:500, Synaptic systems #160 006), Mouse anti-Bassoon (1:500, Abcam # AB82958), Rabbit anti-Synaptophysin (1:500, abcam, #ab32127) Chicken anti-GFP (1:2000, abcam, #ab13970), Mouse anti-Rac1-GTP (1:200, New east Bio, 26903) and Mouse anti-RhoA-GTP (1:400, New east bio, 26904). Secondary antibodies were Alexa Fluor 488 goat anti-rabbit (1:400, Invitrogen # A-11008), Alexa Fluor 405 goat anti-Rat (1:400, Invitrogen # A48261) and Donkey anti-Rat 488 (1:400, Invitrogen # A-21208), Alexa Fluor 647 Goat anti-mouse (1:500, Invitrogen # A-21235), Alexa Fluor 647 Goat anti-chicken (1:500, Invitrogen # A-32933) and Goat anti-rabbit Alexa Fluor 647 (1:400, Invitrogen, #A21244).

Confocal microscopy of fixed brain tissue

Images of fixed brain slices for microglia morphological reconstructions were acquired using a confocal microscope and a 40× oil objective (SP5, Leica) and for microglia density using an epifluorescence microscope (DM6000, Leica). Images for dendrite reconstructions were acquired on a confocal microscope equipped with an Airyscan detector (Zeiss LSM800, Carl Zeiss Microscopy GmbH), using a 63× oil objective. To image tdTomato-expressing dendrites, excitation of tdTomato was achieved by a 561nm laser and emission was collected using a 567–700 nm bandpass filter. Image stacks of visible isolated dendrite fragments of layer II-III pyramidal neurons were acquired with a pixel size of 0.049 μm, a z-step size of 0.200 μm and at a scan speed of 2.55μs/pixel. Images acquired with the Airyscan detector were processed by the ZEN software internal algorithm that reassigns the collected pixels to their correct positions to achieve a super-resolution image; for this a super-resolution threshold of 2 was used.

Images of brain slices for active Rac1 and RhoA quantifications were acquired using a confocal microscope (LSM800, Carl Zeiss AG) and a 40× oil objective (1.4NA, Carl Zeiss AG).

Fluorescent emissions were subsequently collected in two different channels, exciting Alexa Fluor 647 with a 640nm laser and an emission filter at 645-700nm and exciting GFP with a 488nm laser, with emission bandpass filtered at 495–550. A 3D FOV with a size of 266.2 × 266.2 × 15.2 μm (x/y/z) was randomly chosen in frontal cortex layer 2 of td-Tomato expressing neurons with a pixel size of 0.26 × 0.26 × 0.4μm (x/y/z).

Images of brain slices stained for synaptic inclusions were acquired using a confocal microscope equipped with an Airyscan detector (LSM900, Carl Zeiss AG), with a 63× oil objective (1.4 NA, Carl Zeiss AG). Fluorescent emissions were subsequently collected in three different channels with an airyscan detector. The first track excited Alexa Fluor 647 for synaptic proteins with a 640nm laser and emission was bandpass filtered at 555-700nm. The second track excited Alexa Fluor 488 to image Iba1-expressing microglia with a 488nm laser and a detection wavelength of 470-584nm. The last channel was acquired with a 405nm laser to aquire CD68 via Alexa Fluor 405 excitaiton and a detection wavelength of 400-505nm. Single microglia were randomly selected in the area of tdTomato-expressing neurons and imaged with a pixel size of 0.04 × 0.04 × 0.3 μm (x/y/z) and with a FOV size of 67 × 67 × 12 μm for Bassoon stainings and 67 × 67 × 9 μm for Homer1 stainings and 59.6 × 59.6 × 5.4 μm for Synaptophysin stainings. Channel alignment (Extended, Translation + Isoscaling) was done in Zen (Carl Zeiss AG) with previously acquired images in the same resolution and FOV size with fluorescent beads, to ensure enhanced overlay of the different wavelength channels for later colocalization analysis. Airyscan processing was also performed in Zen with a 3D filter of 7.5 (Carl Zeiss AG). Five different FOVs were taken from two different brain slices for each individual animal. Data analysis was performed under blinded conditions.

Reconstruction of synaptic inclusions within microglial cells

For the analysis of synaptic inclusions, images were reconstructed and analyzed using IMARIS software (Bitplane AG, Zürich). Microglia and CD68$^+$ structures were reconstructed in three dimensions utilizing the Surfaces tool. Synaptic inclusion puncta labeled for Homer1 and Bassoon, were identified and reconstructed with the Spots tool. For the classification of CD68$^+$ structures within microglia and for the classification of synaptic puncta within microglial CD68$^+$ structures, a shortest distance classifier was used, with a threshold of 90% for the surface or the puncta having to be inside the colocalized surface. Data analysis was performed under blinded conditions.

Surveilled volume analysis

Two-photon acquired time-lapse images of microglia were reconstructed in IMARIS (Bitplane AG, Zürich). All microglial cells including their processes were reconstructed using the Surfaces tool, thresholds were manually adjusted for each field of view over all time frames. The percentage of microglia surveilled volume was calculated using the total microglial surface volume divided by the full volume of the field of view and averaged over time. Data analysis was performed under blinded conditions.

Reconstruction of dendritic fragments

Image stacks were 3D reconstructed in IMARIS (Bitplane AG, Zürich). The dendritic fragments and associated spines were reconstructed semi-automatically using the Filament Tracer module. Spines that extended radially from the dendrite in three dimensions were drawn manually by turning the 3D visualized dendritic fragment. Filament parameters (small diameter = 0.05 μm, large diameter = 0.80 μm and contrast threshold = 0.100) were defined empirically by measuring a random set of acquired images and comparing the rendered filament with the pre-processed image. Spine density per dendritic fragment and morphological parameters of spines (ratio of mean head to neck diameter, maximum head diameter and spine length) were measured, exported for further analysis (Cluster analysis) and plotted in a 3D graph. Data analysis was performed under blinded conditions.

Cluster analysis

The cluster analysis was performed as previously described.[51] The spine parameters, ratio of the mean head to neck diameters (ØHead/ØNeck), the maximum head diameter (Ømax Head) and spine length were taken into account. Agglomerative Hierarchical Clustering Analysis (AHC) was performed using Python's scikit-learn toolbox. Before cluster analysis, the parameters were centered and scaled to unit variance using the standard scaler from Python's scikit-learn toolbox. AHC dissimilarity level was calculated based on Euclidean distance. Agglomeration was performed using Ward's method. By fitting the hierarchical clustering to the population of all analyzed spines we identified three clusters.

Western immunoblotting

WT and CR3 KO were sacrificed at P17 for immunoblotting analysis. The frontal cortices were dissected, snap frozen and kept at −80°C until processing. Tissues were lysed in 10 vol RIPA lysis buffer (Thermo Pierce, 89900, US) containing protease and phosphatase inhibitors, before being manually homogenized, incubated for 25 min on ice and centrifuged (14 000 rpm for 20 min at 4°C). The supernatants were mixed with Laemmli Sample Buffer (1:1) and equivalent amounts of proteins were resolved by electrophoresis on

8%-, 10%-, or 13% SDS-polyacrylamide gel. Dependent on protein of interest and antibody, 15–30 μg of protein were loaded. Resolved proteins were transferred to Immobilon-FL PVDF Membranes (Merck Millipore, IPFL00010) in 0.1 M Tris-base, pH 8.3, 0.192 M glycine and 20% (v/v) methanol using an electrophoretic transfer system (Bio-Rad). The membranes were blocked by using Odyssey blocking buffer. After blocking, the membranes were incubated 12-72h (+4°C) with primary antibody based on the requirement of the experiment (Table S3). Incubations were followed by washing (TBS-T) and incubation with the goat anti-rabbit IR-Dye 800 CW (1:10 000, Li-Cor Biosciences #926–32211) or goat anti-mouse IR-Dye 680 LT (1:40 000, Li-Cor Biosciences #926–68020) for 1 h at room temperature. Immunoreactive bands were detected by using the Odyssey Infrared Imaging System (Odyssey CLx, Li-Cor Biosciences). To normalize immunoreactivity of the proteins, β-actin was measured on the same blot by using a rabbit or mouse monoclonal anti-β-actin antibody (1:1000 Li-Cor Biosciences #926–42210, or 1:10 000 Sigma-Aldrich #A2228, respectively) followed by incubating with a goat anti-rabbit IR-Dye 680 LT (1:40 000, Li-Cor Bioscience #926–68021) or goat anti-mouse IR-Dye 680 LT (1:40 000, Li-Cor Biosciences #926–68020). For determination of signal intensities, the software Image Studio Lite 5.2. (LiCor Biosciences) was used. The ratio of proteins of interest to β-actin were calculated and expressed as % of control (wild-type group) ± SEM.

Microglial cell density

To evaluate Iba1+ microglial cell density in the frontal cortex, images were acquired using an epifluorescence microscope (DM6000, Leica) on fixed sagittal slices from P15-19 electroporated mice. Quantifications were based on image acquisitions obtained in layer I to III (cortical depth was from the pial surface to ~300 μm below the pial surface) in regions containing electroporated, tdTom+ pyramidal cells. For each individual mouse, microglial cell density was established by the average value obtained in three to four different regions of interest (ROIs). Iba1+ cells were identified and counted using the Cell counter plugin for ImageJ. Data analysis was performed under blinded conditions.

Cranial window surgery

Cortical window surgery was performed at P15-P19 and as previously described.[10] Briefly, mice were anesthetized with an i.p. injection of ketamine/xylazine (0.13/0.01 mg/g body weight). As an analgesic, mice received buprenorphine (0.1 mg/kg; subcutaneously (s.c.), Reckitt Benckiser) shortly before surgery. The body temperature was maintained with a heating pad at 37°C. After fixation in a stereotaxic frame, the skin was removed under aseptic conditions. Using epifluorescence, the hemisphere with C4 overexpression was visualized and confirmed. A craniotomy above the frontal cortex stretching over both hemispheres (2 × 4 mm in size; +3 mm AP, +2 mm ML bilaterally) was performed with a dental drill. The dura was carefully removed. The brain surface was rinsed with sterile saline, and #1 coverslips were placed into the craniotomy sealed with dental cement at the edges. To allow stable and repetitive fixation of the mouse under the microscope, a small metal bar was attached next to the cortical window using UV-curable dental adhesive.

In vivo two-photon imaging

Two-photon imaging was performed right after surgery at a Zeiss 7MP multiphoton microscope with a water immersion Zeiss 20× objective (NA = 1.0; WD = 1.8 mm). The mouse was fixed to a custom-made head-holder and mounted under the microscope on a heating plate to keep the body temperature at 37°C. TdTomato and GFP fluorescence were excited at 980 nm using an InSight X3 tunable laser (Spectra-Physics) and collected through a 525/50 nm band-pass and 617/73 nm band-pass filter with a 550 nm long-pass beamsplitter on a highly sensitive non-descanned GaSP-detector. Time-lapse images were acquired at 125 × 125 μm^2 in x, y-direction with a pixel size of 0.01 μm/pixel. The z-steps were 1 μm spaced and spanned 60 μm. The same stack was acquired every 5 min for a duration of 40 min.

QUANTIFICATION AND STATISTICAL ANALYSIS

Microglial motility analysis

In general, microglial motility was analyzed as described before.[17,52] Expanding from manual analysis we implemented a custom analysis pipeline written in Python. First, noise was removed by applying a median-filter with a kernel size of 3 x 3 pixels. The individual consecutive time lapses of one mouse were maximum intensity projected along the z axis and rigidly registered on each other using subpixel image registration by cross-correlation[53] provided by the open-source Python image processing library Scikit-image.[54] Subsequently, the registered z-projections were binarized by thresholding the pixels in each projection using Otsu's method.[55] The thresholding was preceded by contrast limited adaptive histogram equalization (CLAHE),[56] also provided by the Scikit-image library, in order to enhance the contrast and, thus, the thresholding in each z-projection. Small blobs of less than 100 pixels were removed from the binarized images. We then calculated the temporal variation ΔB(ti) of each binarized image by subtracting the binarized image B(ti+1) at time point ti+1 from two times the binarized image B(ti) at time point ti: ΔB(ti) = 2×B(ti+1)- B(ti) for i = 0, 1, 2, …, *N*-1, where N is the total number of all lapse time points. Pixels in ΔB(ti), that have the value 1, were categorized as stable pixels, whereas pixels with the value −1 were categorized as gained pixels, and pixels with the value 2 as lost pixels. The microglial fine process motility was assessed by calculating the turnover rate (TOR) as the ratio of the number of all gained pixels Ng(ti) and all lost pixels Nl(ti) divided by the sum of all pixels: TOR(ti) = (Ng(ti)+ Nl(ti))/(Ns(ti) + Ng(ti)+ Nl(ti)), where Ns(ti) is the number of all stable pixels. The average turnover rate ("TOR") was calculated by averaging TOR(ti) over all N-1 time lapse time points. Data analysis was performed under blinded conditions.

Analysis of microglia-synapse and microglia-dendrite contacts

Datasets were blinded prior to analysis by an experimenter not involved in the image analysis. In each animal 3–5 dendrites of 30 μm length were analyzed. Spines that extended out laterally from the dendritic shaft were counted manually by scrolling through the z stack, as previously described.[57] Putative boutons were counted similarly, with boutons expanding in $\geq$2 focal planes and extending $\geq$0.4 μm laterally from the axon. Spine and bouton density were calculated as the number of spines divided by the length of the respective dendrite or axon in micrometer. Putative physical contacts of microglial processes and dendritic spines, or microglial processes and axonal boutons, were counted by manually scrolling through the z stack. If fluorescence in both channels was colocalized, this was counted as a contact. Colocalization was defined as fluorescent signals less than $\leq$0.4 μm away from each other in the same focal plane and detectable in $\geq$2 focal planes. Each individual spine or bouton was checked for microglial contacts. Putative contacts were analyzed for every time point during imaging sessions (z-stacks were spaced by 5 min each). To quantify microglia-dendrite interactions along dendritic shafts, the following method was employed: each dendrite was divided into segments, each measuring 1 μm in length. From these segments, three were randomly selected using Research Randomizer (https://www.randomizer.org/). These chosen segments were then examined to determine the presence of microglia contact in each, for every time point during imaging sessions. Data analysis was performed under blinded conditions.

Statistics

Data are presented as mean ± SEM. Statistical analyses were performed using Prism (GraphPad). The normality of data distribution was tested using the Shapiro-Wilk test and the Kolmogorov-Smirnov test. Unpaired two-tail t-tests (for normally distributed datasets) or Mann–Whitney tests (for non-normally distributed datasets) were used for comparisons between two groups. For multiple comparisons we used Sidak's tests (for normally distributed datasets) and Dunn's multiple comparison tests (for non-normally distributed datasets). Effect sizes are reported as Cohen's d. For parametric tests Cohen's d was computed from pooled standard deviations using the t statistics. For non-parametric tests, Z-based effect sizes (r) were converted to Cohen's d using the standard transformation. Of note, we did not analyze the impact of CR3 KO independently of C4-OE, which would necessitate a comparison between CR3 wild-type (WT) and CR3 KO groups, or between Cx3cr1-GFP and Cx3cr1-GFP::CR3 KO groups. This analysis was omitted due to the fact that these experimental cohorts were not derived from the same litters. Values of $p < 0.05$ were considered statistically significant. p values are reported as follows: *$p < 0.05$; **$p < 0.01$; ***$p < 0.001$: ****$p < 0.0001$. Detailed information regarding the statistical analyses (statistical tests used, p values, Cohen's d, number of animals, number of cells) is provided in Tables S1, S2, S3, S4, S5, S6, and S7 of the Supplemental Information.